

Large Area Mapping at 850 Microns. IV. Analysis of the Clump Distribution in the Orion B South Molecular Cloud

Doug Johnstone^{1,2}, Henry Matthews³, and George F. Mitchell⁴

ABSTRACT

We present results from a survey of a 1300 arcmin² region of the Orion B South molecular cloud, including NGC 2024, NGC 2023, and the Horsehead Nebula (B33), obtained using the Submillimetre Common-User Bolometer Array (SCUBA) on the James Clerk Maxwell Telescope. Submillimeter continuum observations at 450 μm and 850 μm are discussed. Using an automated algorithm, 57 discrete emission features (“clumps”) are identified in the 850 μm map. The physical conditions within these clumps are investigated under the assumption that the objects are in quasi-hydrostatic equilibrium. The best fit dust temperature for the clumps is found to be $T_d = 18 \pm 4$ K, with the exception of those associated with the few known far infrared sources residing in NGC 2024. The latter internally heated sources are found to be much warmer. In the region surrounding NGC 2023, the clump dust temperatures agree with clump gas temperatures determined from molecular line excitation measurements of the CO molecule. The bounding pressure on the clumps lies in the range $\log(k^{-1} P \text{ cm}^3 \text{ K}^{-1}) = 6.1 \pm 0.3$. The cumulative mass distribution is steep at the high mass end, as is the stellar Initial Mass Function. The distribution flattens significantly at lower masses, with a turn-over around 3 – 10 M_\odot .

Subject headings: infrared: ISM: continuum - ISM: clouds - ISM: individual (NGC 2024, NGC 2023, B33, Orion B South) - ISM: structure - stars: formation

¹National Research Council Canada, Herzberg Institute of Astrophysics, 5071 West Saanich Rd, Victoria, BC, V9E 2E7, Canada; doug.johnstone@nrc-cnrc.gc.ca

²Department of Physics & Astronomy, University of Victoria, Victoria, BC, V8P 1A1, Canada

³National Research Council Canada, Herzberg Institute of Astrophysics, Dominion Radio Astrophysical Observatory, Box 248, Penticton, BC, V2A 6J9, Canada; henry.matthews@nrc-cnrc.gc.ca

⁴Department of Astronomy and Physics, Saint Mary’s University, Halifax, NS, B3H 3C3, Canada; gmitchell@ap.stmarys.ca

1. Introduction

This paper continues an effort to quantify the necessary pre-conditions for star formation via observations of the continuum emission from cold dust at submillimeter wavelengths. Such observations allow the determination of the mass spectrum and physical characteristics of the population of cold (typically 10–30 K), dense concentrations of dust, or “clumps”, each of which is expected to be a site of active, or eventual, star formation. It is also well known that stars form in groups (see e.g. Clarke et al. 2000, Elmegreen et al. 2000) and that these in turn originate from a hierarchy of dust clumps for which the mass spectrum is closely similar to the stellar initial mass function (IMF; see e.g. Motte et al. 1998; Johnstone et al. 2000b, hereafter Paper II; Johnstone et al. 2001, hereafter Paper III; Motte et al. 2001). The recently launched Spitzer Space Telescope will observe many star-forming regions in the infrared and thus provide information on which dust and gas clumps contain deeply embedded protostars. Together, the submillimeter continuum dust maps and the infrared images will yield statistics on the number of prestellar, Class 0, and Class I protostars and significantly enhance our understanding of the lifetime in each stage and the changes in natal environment with protostellar phase.

Previous papers in this series on large area mapping at $850\ \mu\text{m}$ have discussed image reconstruction techniques (Johnstone et al. 2000a, hereafter Paper I), and results for the Ophiuchus cloud (Paper II) and the northern part of the Orion B region (Paper III). In the present paper we turn our attention to the southern part of the Orion B molecular cloud (Lynds 1630). This region includes a number of objects well known to both amateur and professional astronomers. In particular, the Horsehead Nebula, B33 (see, e.g., Pound et al. 2003), is seen in silhouette against the bright background of the HII region IC 434 near the three bright stars of Orion’s Belt. At a distance of approximately 400 pc [Anthony-Twarog (1982) measured a distance of 390 pc] the Orion B South region also contains the young star clusters NGC 2023 and NGC 2024, and as part of the greater Orion Molecular Cloud is well-known as one of the nearest extensive regions of active star formation. An optical image showing most of the region discussed in this paper, and its relationship with the ionizing stellar system σ Orionis, is given by Abergel et al. (2002).

One of the first systematic searches for dense molecular cores in the Orion B region was carried out by Lada et al. (1991a; hereafter LBS) using the CS $J = 2-1$ transition, for which the effective critical density is about $10^4\ \text{cm}^{-3}$ (Evans 1999). With a beamwidth of $1.8'$ a total of 42 dense cores were found to be concentrated in two relatively small regions of the Orion B molecular cloud; 19 of these lie within the region surveyed in the present paper. Seven of the latter objects were subsequently mapped by Launhardt et al. (1996) at $1300\ \mu\text{m}$ wavelength with an angular resolution of $12''$, comparable to that of the present

observations with the JCMT. From these surveys it is evident that active star formation is confined to two rather limited areas within the Orion B region.

The region has been surveyed at many wavelengths. Early $2.2\ \mu\text{m}$ observations of a large part of the molecular cloud made by Lada et al. (1991b) identified four embedded star clusters, and subsequent widefield imaging of the stellar component is available via the 2MASS images (Carpenter 2000). The distribution of relatively warm dust was mapped by IRAS, although for our purposes with limited angular resolution, and in far infrared emission at 138 and $205\ \mu\text{m}$ (Mookerjea et al. 2000). The molecular component has been surveyed by a number of authors, e.g. Miesch and Bally (1994) in the ^{13}CO $J = 1-0$ transition, and by Kramer et al. (1996) with lower angular resolution in the ^{13}CO and ^{12}CO $J = 2-1$ and $3-2$ transitions.

The Horsehead Nebula in particular has been extensively investigated. Pound et al. (2003) have obtained an interferometric image in the CO $J = 1-0$ transition of the Horsehead Nebula with an angular resolution of $10''$. Abergel et al. (2003) combine mid-infrared ISOCAM data in the LW2 and LW3 bands with CO , ^{13}CO and C^{18}O $1-0$ and $2-1$ observations to model the transient heating of the outer edge of the dust cloud by photodissociating radiation from the relatively nearby O9.5V system σ Orionis. Teyssier et al. (2004) have obtained detailed observations of simple cyclic and linear hydrocarbons, which they show to be distributed similarly to CO within the western edge of the nebula. Finally, early results from submillimeter-wavelength mapping of the Horsehead Nebula region have been reported by Sandell et al. (2001); these latter archival data have been included in the dataset for the present work, which covers a total area about $1300\ \text{arcmin}^2$ in extent.

2. Observations and Data Reduction

The data covering Orion B South were obtained between 1997 and 2000 using SCUBA at the JCMT. The JCMT archive, hosted by the CADC¹, was used to find all relevant observations toward the region. A total of 135 individual scan and jiggle maps were retrieved, which, when combined, cover a total observed area of $1300\ \text{arcmin}^2$. Each individual 3-arcsec cell in the final data array was measured approximately 40 times at $850\ \mu\text{m}$ and 90 times at $450\ \mu\text{m}$. Thus, the total time spent observing each cell was approximately 5 and 11 seconds respectively. The weather conditions varied significantly during the many nights of observing. The mean optical depths at $850\ \mu\text{m}$ and $450\ \mu\text{m}$ were on average quite favorable,

¹The Canadian Astronomy Data Centre (CADC) is operated by the Dominion Astrophysical Observatory for the National Research Council of Canada's Herzberg Institute of Astrophysics.

$$\tau_{850} = 0.26 \pm 0.07 \text{ and } \tau_{450} = 1.4 \pm 0.4.$$

The raw bolometer data were reduced using the standard SCUBA software (Holland et al. 1999) to flat-field, extinction correct, and flux calibrate. The extinction corrections and flux calibrations as a function of time were obtained from the JCMT calibrations archive (Jenness et al. 2002). The extinction corrections are tabulated as a function of time based on a comparison of skydip measurements taken with the JCMT during normal observing and zenith optical depth measures taken every few minutes at 225 GHz by the CSO tau meter. The flux calibration values are tabulated from all calibration measurements taken during extended periods of time, e.g. semesters, over which the telescope and instrument were not known to have changed significantly. Typical uncertainties in the flux calibration can be determined from Jenness et al. 2002 (see their Figures 1 and 2). At 850 μm the uncertainty is approximately $\pm 10\%$ while at 450 μm the uncertainty is closer to $\pm 25\%$. These values are consistent with the uncertainties determined by individual observers using calibrator sources. Most of this uncertainty is due to changes in the telescope surface due to temperature and gravity during the night and resultant changes in the beam profile, which can be quite significant at 450 μm .

The data were further reduced and transformed into the final maps using the matrix inversion technique described in Paper I. This method has many advantages over the standard facility data reconstruction procedure, in particular the ability to use all data taken at the telescope, regardless of chop configuration or mapping procedure, and the ability to properly weight each individual measurement based on bolometer and sky noise. Significant low-amplitude, large-scale features remain after reconstruction and may be real; however, artificial features produced by weather variations and bolometer drift over time will also produce this type of structure since reconstruction of chopped data amplifies the longer spatial wavelengths (chop throws range from 20" to 65"). We filter out these large-scale features by convolving the map with a large Gaussian profile ($\sigma = 135''$) and subtracting the resultant smoothed map from the reconstruction. In order to minimize the effect of over-subtraction in regions with bright sources, all pixels greater than 0.25 Jy beam⁻¹ at 850 μm and 5 Jy beam⁻¹ at 450 μm have been removed in the construction of the smoothed map. The final, reconstructed 850 μm and 450 μm maps, after filtering, are shown in Figures 1 and 2 along with maps of the estimated uncertainty at each position. Note that the uncertainty in the measurement drops significantly in regions where multiple observations were made, such as the Horsehead region.

3. Data Analysis: Clump Properties and Distribution

3.1. Identification of Clumps

We have noted that size scales significantly larger than the maximum chop throw are unlikely to be correctly registered in the final images, and such structures have been removed. The data are thus amenable to an automated clump-finding analysis for structures of size scales up to approximately $130''$.

Clumps within the Orion B South region were identified in substantially the same manner used for Ophiuchus (Paper II) and Orion B North (Paper III), allowing for a direct comparison of the results. The flattened $850\ \mu\text{m}$ map was searched for structure using a two-dimensional version of the clump-finding algorithm, `clfind` (Williams et al. 1994). This algorithm divides the map into individual clumps by utilizing minimum flux boundaries, assigning each cell in the map above a limiting threshold to a particular clump. Thus, unlike Gaussian clump-finding algorithms, the regularity of a clump is not preset and clumps are allowed to have arbitrary shapes. A comparison of this clump-finding algorithm and “by eye” techniques is discussed in Paper III, where it is shown that the two techniques produce very similar results; however, with no observer bias in the present case.

The typical sensitivity in the raw map is similar to that found in Paper III, about $40\ \text{mJy}$ per pixel, or $10\ \text{mJy}$ per beam at $850\ \mu\text{m}$. Comparison can also be made with the millimeter-wavelength maps of Orion B produced by Launhardt et al. (1996) which had a sensitivity of approximately $130\ \text{mJy}$ per $30''$ beam. Assuming the dust opacity scales as ν^2 the mass sensitivity of the Launhardt observations is about sixteen times less good than in the present work. In order to maintain a uniform clump sensitivity across the map, the typical noise value in the flattened map, approximately $30\ \text{mJy}$ per pixel, was used as input to `clfind`.

Initially, 69 clumps were obtained by the `clfind` routine; however, twelve were removed due to location within the map, leaving 57 clumps. All removed clumps were near the edges of the map where residual noise is highest. Following Papers II and III, the size of each clump was computed by taking the area of each clump and determining the “effective radius” of a circle with equivalent extent. It should be noted, however, that a number of the clumps deviate significantly from circular symmetry. The properties of the 57 clumps are presented in Table 1 and the locations and relative sizes of the clumps are shown in Figure 3. The total flux for each clump has not been corrected for the effect of the telescope error beam, in keeping with previous papers in this series. The error beam at $850\ \mu\text{m}$ is at most $\sim 10\%$, much less significant than the calibration uncertainty.

An initial estimate of the mass for each clump was computed from the total flux within the clump boundary under the assumption that the measured flux was due to thermal emission from optically thin dust particles (c.f. equation 1 in Paper III):

$$M_{\text{clump}} = 0.59 \times S_{850} \left[\exp \left(\frac{17 \text{ K}}{T_d} \right) - 1 \right] \left(\frac{\kappa_{850}}{0.02 \text{ cm}^2 \text{ g}^{-1}} \right)^{-1} \left(\frac{d_{\text{OriB}}}{400 \text{ pc}} \right)^2 M_{\odot}. \quad (1)$$

Following the results of van der Tak et al. (1999) we take the opacity per unit mass column density at $850 \mu\text{m}$ to be $\kappa_{850} = 0.02 \text{ cm}^2 \text{ g}^{-1}$, a factor of two higher than that used in our previous papers. The distance to Orion B South is assumed to be $d_{850} = 400 \text{ pc}$, somewhat less than the 450 pc distance used in Paper III for Orion B North. Anticipating the results of the detailed analysis below, the typical dust temperature for each clump is taken to be $T_d = 20 \text{ K}$, producing clump masses in the range 0.37 to $90 M_{\odot}$. The four most massive clumps are atypical however; they are coincident with known far infrared sources (Mezger et al. 1988) and have much higher dust and gas temperatures, $T_d > 50 \text{ K}$ (Mangum, Wootten, & Barsony 1999; Fissel et al. 2005). For these four sources the derived masses are substantially decreased if the higher temperature is adopted, lowering the maximum clump mass found in Orion B South to less than $30 M_{\odot}$. The derived mass versus size relation for the clumps is plotted in Figure 7, assuming $T_d = 20 \text{ K}$ for *all* clumps.

In Paper III, the clumps in Orion B North were assumed to have a lower value of κ than used here, and a higher typical dust temperature, $T_d = 30 \text{ K}$. As well, the distance was taken to be 450 pc rather than 400 pc . To compare derived masses between Paper III and this paper on a uniform scale, multiply by 0.7 the masses quoted in Paper III.

3.2. Clump Distribution

Within the Orion B South region the three objects B33 (also known as the Horsehead Nebula), NGC 2024, and NGC 2023 contain the large majority of the star-forming activity and submillimeter-wavelength emission clumps discussed in this paper. We present expanded images of these regions at 850 and $450 \mu\text{m}$ from the present work, in each case together with a corresponding optical image from the Digitized Sky Survey (DSS) and the $8\text{-}\mu\text{m}$ image obtained by the MSX satellite (Price et al. 2001).

3.2.1. The Horsehead Nebula

Of the three regions, only B33 presents aspects common to all wavelengths (Figure 4). The top of the Horsehead “neck” and “head”, which provide a sharp boundary to the dark

cloud silhouetted against the bright background of the optical emission nebula IC 434, is revealed as a region of cold dust at submillimeter wavelengths. The western edge, heated by σ Orionis further to the west (Abergel et al. 2003), appears bright at $8\ \mu\text{m}$, and contains a compact feature at mid-IR wavelengths which could be a prestellar object. The latter is not differentiated at sub-mm wavelengths.

The clump-finding routine identifies two $850\ \mu\text{m}$ sources (054089-02271 and 054091-02278; see Table 1), both parts of the “horse’s mane”, in this region, but neither are specifically associated with the compact mid-IR feature noted above. Both clumps have moderately cool submillimeter-wavelength dust temperatures (Table 2). A third bright dust clump (054112-02273) $3'$ to the east, within the “horse’s neck”, has no obvious counterparts at mid-IR or optical wavelengths, but is amongst the warmer sources based on the submillimeter data (see Table 2). Other submillimeter sources further to the east are parts of a clumpy ridge of emission extending south from NGC 2023. Mid-IR emission possibly associated with this ridge is displaced slightly to the west, and likely results from heating by σ Orionis.

3.2.2. NGC 2023

Optical and mid-IR images of NGC 2023 bear no resemblance to the submillimeter-wavelength images (see Figure 5), and very little to each other. The optical image is dominated by a bright reflection nebula with some patchy absorption by foreground dust. The illuminating star for the reflection nebula is HD 37903; heated dust gives rise to the structure shown in the $8\text{-}\mu\text{m}$ MSX image and also in ISOCAM data (Abergel et al. 2002). The submillimeter-wavelength data however reveal a strongly clumped structure containing 12 individual components. Comparison with the LBS dataset shows that three CS clumps lie within NGC 2023. LBS 34 can be identified with the submillimeter clump 054162-02172, while 054142-02160 is likely to be related to LBS 36. Interestingly, no LBS clump is identified with the brightest continuum source in NGC 2023, 054141-02180; this object is known to harbor a very cold Class 0 source with a well-collimated molecular outflow (see Reipurth et al. 2004, and references therein). The remaining LBS clump within the field in Figure 5, LBS 39, is not clearly associated with compact submillimeter continuum emission.

3.2.3. NGC 2024

As a major star formation region NGC 2024 has been extensively studied. As shown in Figure 6 (upper right panel) the optical appearance is of an extensive ionized region overlaid

with a dense foreground dust lane; the visual extinction toward the deeply-embedded object IRS 2 (Grasdalen, 1974) has recently been determined as ≥ 27 mag at $2.2 \mu\text{m}$ (Lenorzer et al. 2004). Although IRS 2 contributes significantly to the ionization, it was known for some time that this star did not meet the O9-O9.5 stellar equivalent required. Recent work by Bik et al. (2003) suggests that a second fainter star, IRS 2b, only $5''$ from IRS 2, actually provides the necessary ionization. Centimeter-wave aperture synthesis continuum observations of this region (Barnes et al. 1989) show an HII region with a sharply-delineated “bay” to the south. This structure cannot be seen at infrared wavelengths, but is replicated in the mid-infrared emission at $8 \mu\text{m}$ (lower left panel, Figure 6).

The submillimeter wavelength observations of NGC 2024 (see Figure 6) show a structure consisting of two major clumps of dust emission bordered by a number of filamentary structures. Earlier millimeter-wave observations by Launhardt et al. (1996) reveal that the two major clumps of emission, as well as the CS clump LBS 33, coincide with this structure. At $633 M_{\odot}$, this is the most massive molecular clump found by Lada et al. (1991) in the Orion B South complex.

The SCUBA observations in this paper identify a total of 16 clumps within the region shown in Figure 6, including the four brightest sources in the map. These objects collectively and individually represent by far the most massive concentration of clumped dust within the entire Orion B South region. Notably, all of these objects have been assigned dust temperatures of 50 K, much higher than the mean dust temperature in the larger region, on the grounds that the 850 and $450 \mu\text{m}$ fluxes are inconsistent with a modified blackbody model. Molecular line observations (Fissel et al. 2005) confirm that the clumps are warm.

4. Modeling Clumps as Bonnor-Ebert Spheres

The nature of the submillimeter-wavelength clumps found in nearby molecular clouds is at present quite controversial. Whether the clumps are long-lived, slowly evolving entities, perhaps the result of a gradual release of magnetic support (Mestel & Spitzer 1956; Shu 1983; Nakano 1984; Shu et al. 1987; Mouschovias & Ciolek 1999; Basu & Ciolek 2004), or transient turbulent structures (Scalo 1985; Mac Low & Klessen 2004 and references therein) has yet to be definitively settled. The recently launched Spitzer Space Telescope will play an important role by determining which clumps have embedded protostars. Regardless, molecular line observations show that the line widths of such dense cores are narrow, indicating that non-thermal motions do not overwhelm the dynamics (Barranco & Goodman 1998; Goodman et al. 1998), and implying that equilibrium models should reasonably reproduce the clump conditions.

In Papers II and III, physical conditions for the clumps were estimated through modeling the observations as Bonnor-Ebert spheres (Ebert 1955; Bonnor 1956; Hartmann 1998). In particular, the observable size R''_{eff} , the flux S_{850} , and degree of concentration C for a Bonnor-Ebert sphere map directly to the physical mass, temperature, and bounding pressure of the object. The concentration is found from the observable size, total flux, peak flux F_{850} , and the FWHM beamsizes B'' (c.f. equation 2 in Paper III):

$$C = 1 - \frac{1.13 B''^2 S_{850}}{\pi R''_{\text{eff}}{}^2 F_{850}}. \quad (2)$$

A number of important assumptions are required when applying this technique to available submillimeter-wavelength data. First, the conversion from flux to temperature requires knowledge of the dust opacity (see above) and the assumption that the dust and gas temperatures are related. Given the high densities for these clumps ($n > 10^4 \text{ cm}^{-3}$) it is reasonable to assume the dust and gas temperatures are similar and thus we take $T_d = T_g$. In a departure from our earlier models, we assume also that an additional turbulent component of pressure exists within the clumps, equal to the thermal pressure at every location. This change in our analysis is motivated by observations by Goodman et al. (1998), where no clumps were found to have less than approximately fifty percent turbulent support using dense gas tracer molecules². Given that the bulk of the molecular cloud has strongly non-thermal support, we take the transition case, equal contributions from both thermal and non-thermal, as an approximation for the clump support. Finally, determination of both the clump boundary (i.e. size) and degree of concentration (i.e. the importance of self-gravity) are complicated by the limited angular resolution and low sensitivity of the observations. Most of the clumps, however, lie well below the concentration at which clumps become unstable (see Figure 8) and thus are well represented by almost constant density models. For these cases, determination of the physical properties, mass, temperature, and bounding pressure are *not* strongly dependent on the determination of the exact value of the central concentration. The clumps with the more extreme concentrations, located in the unstable part of the diagram, are marked with diamonds in Figure 8. The known far infrared sources lie among this group.

Applying the Bonnor-Ebert sphere analysis used in Papers II and III, the physical conditions for each clump are plotted in Figure 9. Excluding the extreme concentration sources (marked by diamonds), the typical clump temperature is $T_d = 18 \pm 4 \text{ K}$. The pressure

²We note, however, that the level of turbulent support may be strongly dependent on the region. Recent results by Tafalla (private communication; see also Tafalla et al. 2004) show that in Taurus the fraction of pressure support due to turbulent motions is much less than fifty percent.

required to bound the clumps is $\log(k^{-1} P \text{ cm}^3 \text{ K}^{-1}) = 6.1 \pm 0.3$. The scatter in T_d and $k^{-1} P$ values is only marginally larger than the uncertainty in any individual source measurement. A comparison with the results of our previous papers must take into consideration the change in the opacity law and the inclusion of additional turbulent support within each clump. Together these changes almost exactly cancel in the determination of the bounding pressure and approximately halve the computed internal temperature. With this in mind, the clump temperatures in Orion B South appear similar to those in Orion B North (Paper III) and somewhat warmer than those in Ophiuchus (Paper II). The bounding pressure is lowest in Orion B and highest in Ophiuchus. As noted in Paper III, this is in general agreement with the known conditions within the clouds; Ophiuchus has a significantly higher central column density, and hence internal pressure, than Orion, where observations have been obtained. In Orion the typical peak extinction through the cloud is 8 magnitudes with a maximum of 17 magnitudes (Lambardi and Alves 2001), whereas in the core of Ophiuchus the peak extinction reaches 36 magnitudes (Johnstone et al. 2004). Thus the Orion molecular clouds are bathed in an enhanced interstellar radiation field which warms the region.

4.1. Clump Temperatures Derived from Submillimeter Colors

In principle, the dust temperature within each clump can be estimated from the submillimeter spectral index, γ , where $S(\nu) \propto \nu^\gamma$. Assuming that the dust opacity follows a power-law with $\kappa(\nu) \propto \nu^\beta$, and that the dust emission can be approximated by a blackbody at temperature T_d , the dust emission is given by

$$S(\nu) \propto \nu^\beta B_\nu(T_d). \quad (3)$$

In practice, however, determining the dust temperature is complicated by the fact that the dust opacity power-law coefficient, β , is poorly constrained and often varies with location and physical conditions (Goldsmith, Bergin, & Lis 1997; Visser et al. 1998; Hogerheijde & Sandell 2000; Beuther, Schilke, & Wyrowski 2004). As well, the $450 \mu\text{m}$ and $850 \mu\text{m}$ beam sizes at the JCMT are significantly different and the $450 \mu\text{m}$ beam is not well approximated by a single Gaussian function (Hogerheijde & Sandell 2000); at least half of the flux in the $450 \mu\text{m}$ beam is associated with a broad component about $30''$ in extent. Thus, simple convolution of the central $8.5''$ $450 \mu\text{m}$ beam with the $14.5''$ $850 \mu\text{m}$ beam will significantly overestimate the contribution of $450 \mu\text{m}$ emission on large scales. A sophisticated solution to determining β is to use a Fourier Transform Spectrometer to produce a low resolution spectrum of the $850 \mu\text{m}$ emission alone. At present, however, this is only possible for very bright sources (Friesen et al. 2005). Here we utilize the $450 \mu\text{m}$ and $850 \mu\text{m}$ emission from SCUBA and follow the approach of Reid & Wilson (2005) in preparing the maps for analysis.

We convolve the 850 μm map with a model of the 450 μm beam and the 450 μm map with a model of the 850 μm beam. For this purpose the 450 μm beam is modeled as two Gaussian components with 8.5'' and 30'' FWHM, and relative peak intensities of 0.95 and 0.05. The 850 μm beam is modeled as two Gaussian components with 14.5'' and 30'' FWHM, and relative peak intensities of 0.95 and 0.05.

Assuming that $\beta = 2$ (Hildebrand 1983), the central dust temperature for each clump was estimated using the total flux in the convolved 850 μm and 450 μm maps by inverting

$$\frac{S_{450}}{S_{850}} = 24 \left[\frac{\exp\left(\frac{17}{T_d}\right) - 1}{\exp\left(\frac{32}{T_d}\right) - 1} \right]. \quad (4)$$

The derived values are provided in Table 2 and a comparison with the derived Bonnor-Ebert model temperatures is shown in Figure 10. It is clear from the figure that while there is qualitative agreement on which clumps are warm, the spectral energy distribution derived temperatures for most clumps are poorly constrained by the available submillimeter-wavelength data. Some of the clumps, particularly at the faint end of the distribution, have 450 μm to 850 μm flux ratios which are inconsistent with modified blackbodies having $\beta = 2$. In Table 2 and Figure 10 we assume that these sources are warm ($T_d = 50$ K), although alternative explanations include $\beta > 2$ and/or measurement unreliability for the derived fluxes. We have already noted in Section 2 that the typical uncertainty in the flux determination at 850 μm is 20% whereas at 450 μm the typical uncertainty is 50% (Jenness et al. 2002), notwithstanding the complication of convolution discussed above. Setting aside the atypical high flux ratio sources, the mean dust temperature of the clumps derived from fitting the spectral energy distribution between 450 μm and 850 μm is $T_d = 18 \pm 6$ K.

Once protostellar source catalogues obtained from Spitzer Space Telescope observations become available for the Orion B South region, a detailed investigation between the observed concentration and temperatures of clumps derived from the continuum observations and the presence of internal sources will be possible, yielding significant improvement in our understanding of the evolution of these prestellar and protostellar envelopes.

4.2. Clump Temperatures Derived from Molecular Line Observations

Mapping of CO isotopomers was carried out at the JCMT during the same observing runs, when sky conditions did not permit continuum observing. Scan maps of part of the Orion B South region, NGC 2023, were obtained in ^{13}CO J = 2–1, C^{18}O J = 2–1, and C^{18}O J = 3–2. The maps are shown in Figures 11, 12, and 13. Figure 14 shows 850 μm continuum

contours overlaid on the C¹⁸O J = 2–1 map. The J = 2–1 maps were acquired using 7.5'' sampling, which is about one third of the 21'' beamwidth. The C¹⁸O J = 3–2 map has a beamwidth of 14'' and was acquired using 5'' sampling.

The ¹³CO to C¹⁸O J = 2–1 line ratio provides the optical depth over the map, on the assumption of LTE. Goldsmith, Bergin, and Lis (1997) find that the abundance ratio, ¹³CO/C¹⁸O, lies in the range 6-15. In the present analysis we assume that the abundance ratio of ¹³CO to C¹⁸O is 10. As expected, the C¹⁸O emission is optically thin, with τ being typically less than 0.1, and ranging up to a maximum of 0.2. In addition to being optically thin, the C¹⁸O J = 3–2 map has the same resolution as the 850 μ m map and so is the most useful for a comparison of dust and gas emission. The C¹⁸O and continuum maps agree quite well in general appearance, but a closer examination shows that the C¹⁸O emission is somewhat smoother, less clumpy, and more extended than the dust continuum emission. These differences might be due in part to the removal of extended continuum emission by the SCUBA chopping technique, in part to different dependence of CO and dust emission on temperature, and in part to the freeze-out of CO molecules onto grains.

We have obtained the CO excitation temperature from the ratio of the two rotational lines of C¹⁸O. The relevant equation is

$$T_{\text{ex}} = 16.59 \log_e \left[\frac{4 I_R(3-2)}{9 I_R(2-1)} \right]. \quad (5)$$

This equation is obtained from standard LTE and optically thin expressions and is derived in Mitchell (1993). Here, I_R is the integrated intensity of the appropriate spectral line, with the line temperature expressed in units of radiation temperature ($T_R = T_A^*/\eta_{mb}$, with the assumption that the beam filling factor is unity). We use appropriate beam efficiencies for the two transitions ($\eta_{mb} = 0.69$ for the 2-1 line and 0.63 for the 3-2 line) and convolve the C¹⁸O J = 3–2 observations to match the 21'' beam of the J = 2–1 data. We find that, for most pixels over the map, the C¹⁸O excitation temperature lies in the range 14 K to 20 K, with a mean of 16 K. The (rare) extreme values are 10 K and 25 K. The uncertainty in individual values, due only to noise in the data, is ± 2 K. These excitation temperatures are quite consistent with the average temperature of 18 ± 4 K found above for clumps in the NGC 2023 region, using a Bonnor-Ebert analysis.

Five of the continuum clumps in Table 1 fall inside the region of NGC 2023 that we mapped in all three CO transitions. Using the continuum positions of these clumps, we have calculated the C¹⁸O excitation temperature from the above equation and the C¹⁸O column density using the expression given by Mitchell et al. (2001). Optically thin values of column density were multiplied by the factor $\tau/(1 - \exp(-\tau))$ to correct for optical depth. The C¹⁸O column density was converted to a H₂ column density using the ratio N(H₂)/N(C¹⁸O)

$= 6 \times 10^6$. In Table 3 we list, for these five continuum clumps, the temperature from the Bonnor-Ebert analysis, the dust temperature from the $850 \mu\text{m}/450 \mu\text{m}$ ratio, the C^{18}O excitation temperature, the H_2 column density derived from the $850 \mu\text{m}$ peak flux per beam (assuming the BE derived temperature), the H_2 column density from the C^{18}O observations, and the ratio of the two column density determinations.

The gas temperatures agree very well with the dust temperatures. This close agreement is rather unexpected in view of the large uncertainties in the two dust temperature techniques. The single exception is 054153-02189, where the dust temperature from the submillimeter continuum ratio is anomalously low. Column densities derived from CO and dust emission agree reasonably well for four of the clumps (054153-02189, 054162-02172, 054167-02171, 054173-02170) but differ by a large factor for one (054141-02180). A similar analysis for 16 clumps in Orion B North (Mitchell et al. 2001) resulted in masses from dust continuum exceeding masses from C^{18}O by factors of a few. The present closer agreement is due in part to the use of a larger grain opacity in this paper.

Freeze-out of CO molecules on grains is a common phenomenon in cold cores (e.g. Jørgensen, Schöier, and van Dishoeck 2005) and could explain the high $\text{N}(850)/\text{N}(\text{C}^{18}\text{O})$ ratio for the one clump. However, since all five clumps have similar temperatures, why has molecular depletion acted in only one of the five clumps? Various uncertainties enter the column density determinations, including the value of the grain opacity and CO isotopic abundances, so that the ratio, $\text{N}(850)/\text{N}(\text{CO})$, could easily be increased by a factor of two or three and become consistent with some CO freeze-out in all cases. An examination of the C^{18}O $J = 3-2$ map shows that obvious clumps are present at only two of the five positions, namely continuum clumps 054141-02180 and 054167-02171. The apparent agreement in the case of the first clump is deceptive, however. The C^{18}O peak is displaced $20''$ to the southeast of the continuum peak. Although there is an extension of $850 \mu\text{m}$ emission from this clump towards the southeast, the clump-finding algorithm did not detect an independent clump at this position. Examination of the higher resolution $450 \mu\text{m}$ map does show a separate peak at the C^{18}O position. In fact, this second peak was detected by Sandell et al. (1999) in an early SCUBA observation. They called this clump 054141-02180 NGC 2023 mm1 and they named the source to the southeast NGC 2023 mm2. The position of the latter source coincides with the C^{18}O peak. From a variety of evidence, including a CO bipolar outflow, Sandell et al. (1999) suggested that NGC 2023 mm1 is a Class 0 YSO. It appears that strong CO depletion has occurred in mm1 but not in mm2. Clump 054167-02171 is bright in both continuum emission and in C^{18}O emission. It is almost certainly significant that this clump is the warmest of the five clumps, with a temperature of 24 K. This is warm enough that CO depletion is not expected to occur (e.g. Figure 1 of Jørgensen et al. 2005).

4.3. The Clump Mass Distribution Function

Stars form inside dense condensations within Giant Molecular Clouds. At least some of the clumps investigated above are expected to form, or to be forming, stars, and thus understanding the physical properties of these clumps and their environment will help constrain formation mechanisms. One important bulk property of the clumps is the distribution of clumped mass. Following the pioneering study of the Ophiuchus molecular cloud complex by Motte et al. (1998), a number of submillimeter-wavelength surveys have been completed, each resulting in essentially the same conclusion, despite the objects found being in different environments. The mass function of the submillimeter condensations (Testi & Sargent 1998; Paper II; Paper III; Motte et al. 2001) essentially mimics the stellar IMF where $N(M) \propto M^{-1.35}$ for stars more massive than $M \sim 0.5 M_{\odot}$ (Salpeter 1955) and the bulk of the mass resides at the low-mass end (Scalo 1986; Kroupa et al. 1993). This result is in direct contrast with the mass function of molecular clouds (Williams & McKee 1997; McKee & Williams 1997; Kramer et al. 1998; Williams, Blitz, & McKee 2000 and references therein) where $N(M) \propto M^{-0.5}$ and the majority of the mass is found in the few large clouds.

As in Papers II and III, the clump mass distribution is plotted in terms of cumulative number $N(M)$ of clumps with masses greater than M . Figure 15 presents the Orion B South data for both a constant flux-to-mass ratio (for $T_d = 20 K$) and for masses calculated using the Bonnor-Ebert sphere analysis. The horizontal dotted lines indicate the possible variation of the distribution due to uncertainties in the Bonnor-Ebert derived temperatures (as discussed in Paper III). The two dashed lines in Figure 15 denote power-law fits with $N(M) \propto M^{-\alpha}$, where $\alpha = 0.5$ (shallow line) or $\alpha = 1.5$ (steep line) and are presented to guide the eye. The cumulative mass function determined using Bonnor-Ebert derived masses is steep, as is the stellar IMF at the high mass end, but flattens significantly around $M \sim 3 - 10 M_{\odot}$. This is in contrast to the clump IMF measured in Orion B North (Paper III) and Ophiuchus (Paper II) using the same technique and with similar sensitivity. In both those distributions the steep mass function continued to $M \sim 1 M_{\odot}$.

One explanation for the observed discrepancy may be the environmental conditions in which the clumps are found. The typical clump in Orion B South is more extended, and thus less dense, than those found in Orion B North or Ophiuchus. The lower density of the clumps may imply a lower bounding pressure, in agreement with the Bonnor-Ebert analysis above. Why the clump mass distribution should be strongly affected by a relatively small change in bounding pressure is, however, unclear. The Jeans' mass at which clumps become unstable varies only with the square root of the bounding pressure. More likely, the effect is due to the sensitivity limits of the survey. The mass versus radius distribution of clumps in Figure 7 reveals that incompleteness in clump identification may already become important

at $M \sim 5 M_{\odot}$, explicitly because the clumps are more diffuse, lower in surface brightness, and thus harder to detect.

There is significant discrepancy between the mass function of structure in molecular clouds derived from molecular line observations (shallow), particularly CO (e.g. Kramer et al. 1998), and submillimeter-wavelength dust continuum radiation (steep). It is important to note that there are exceptions to this trend. Onishi et al. (2002) identified clumps within Taurus using H^{13}CO^+ $J = 1-0$ line emission and found a steep mass function. Also, Kerton et al. (2001) and Mookerjee et al. (2004) have found much shallower mass functions associated with larger, more massive dust continuum clumps in distant Giant Molecular Clouds. These latter submillimeter-wavelength structures are most definitely the counterparts to the dense cores typically observed in molecular line emission, while the H^{13}CO^+ clumps are counterparts to the small-scale, dense dust continuum structures discussed in this paper. It remains to be determined, however, whether there is a clear separation between these two types of structure or whether the different observing techniques are presently sensitive only at the extremes of an underlying smoothly varying distribution.

4.4. Clump Environment

The cold dust clumps found are grouped in three main concentrations: B33, NGC 2024, and NGC 2023. These regions were also observed to be bright in line emission; for example, in addition to CO and its isotopomers, CS $J = 2-1$, traditionally a dense gas tracer (LBS). Figure 16 overlays the integrated CS observations on the $850 \mu\text{m}$ image for comparison. As in Orion B North (Paper III), the vast majority of the submillimeter-wavelength clumps lie above the 3 km s^{-1} contour, corresponding to column densities of $N_H \sim 10^{22} \text{ cm}^{-2}$ through the CS core region. This is consistent with the result that an extinction threshold may exist for the formation of smallscale, thermally dominated, submillimeter clumps (Paper II, Paper III, Johnstone, Di Francesco, & Kirk 2005). There are, however, two distinct clumps (SMM J054204-02077 and SMM J 054205-02025) residing in particularly low integrated CS emission. Both of these sources are highly concentrated but otherwise unremarkable.

Johnstone et al. (2005) noted that approximately twenty percent of the mass of the core region in Ophiuchus has fragmented into identifiable submillimeter clumps. The apparent threshold for submillimeter clump formation, however, leads to few sources being detected outside the dense core and thus only two percent of the mass of the entire Ophiuchus cloud is visible as submillimeter clump fragments. These are intriguing numbers, comparable to the fractional mass of embedded young clusters in dense cores (Lada & Lada 2003), suggesting that the clumping process may be linked to the formation of stellar associations.

Comparing the CS mass determinations of the parent cores, derived by LBS, against the total submillimeter clump mass residing within each core for both Orion B South and Orion B North (Paper III) is straightforward. Although there exists a significant spread from 5% mass fragmentation in NGC 2071 to 35% mass fragmentation in NGC 2024, overall one finds $\sim 300 M_{\odot}$ in submillimeter clumps within $\sim 1700 M_{\odot}$ of CS clumped material, or approximately 20 percent fragmentation by mass. This result is identical to that found for the Ophiuchus region.

5. Conclusions

We have presented images of the southern part of the Orion B region obtained at submillimeter wavelengths of 850 and 450 μm , covering an area 1300 arcmin² in extent. Utilizing the techniques developed in Papers I, II, and III, we have identified 57 independent dust concentrations, or “clumps”, within this region. The majority of these clumps are concentrated in two star-forming regions, NGC 2024 and NGC 2023; a third minor grouping appears in the Horsehead Nebula cloud. Most of the dust mass is concentrated in NGC 2024.

We have been able to derive estimated masses and temperatures for the majority of the clumps by noting that they can be modelled as Bonnor-Ebert spheres; that is, they can be approximated by almost constant density models with low internal velocities. On this basis the typical clump temperature is found to be 18 ± 4 K; this value is in reasonable agreement with that (21 ± 9 K) derived from the spectral indices obtained from the 850 and 450 μm data. Thus for most of the clumps a temperature of 20 K is a good working approximation. However, 9 clumps are centrally concentrated enough that they may be collapsing, and 4 of these objects are particularly bright at 850 μm . All of the latter lie within NGC 2024 and have temperatures which are considerably higher than that for the majority of the clumps.

Using CO isotopomer spectral line data obtained for NGC2023 we have attempted to obtain independent estimates of temperatures and masses for the clumps in this particular region. With one exception the results obtained agree with those derived from the continuum data. It can be difficult, however, to clearly relate CO structures with equivalent continuum clumps. This problem becomes more acute at the lower mass end of the clump distribution, where continuum sensitivity is limited and individual clumps overlap.

The mass function of submillimeter clumps found in Orion B South is steep, in agreement with the results in other nearby regions (Motte et al. 1998; Paper II; Paper III; Motte et al. 2001). The fraction of mass in each CS-identified core which has fragmented in observable submillimeter clumps is ~ 20 percent.

The research of D.J. and G.M. is supported through grants from the Natural Sciences and Engineering Research Council of Canada. Thanks to John Bally for supplying the CS data and lengthy conversations. Thanks also to Rachel Friesen and Helen Kirk for critical readings and to the anonymous referee for comments that improved this paper. We wish to acknowledge our collaborators in this JCMT key project survey of molecular clouds: Lorne Avery, Shantanu Basu, Mike Fich, Jason Fiege, Gilles Joncas, Lewis Knee, Brenda Matthews, Ralph Pudritz, Gerald Schieven, and Christine Wilson. We thank Tim Jenness and Dave Berry for help with converting one of the figures. The JCMT is operated by the Joint Astronomy Centre on behalf of the Particle Physics and Astronomy Research Council of the UK, the Netherlands Organization for Scientific Research, and the National Research Council of Canada. The authors acknowledge the data analysis facilities provided by the Starlink Project which is run by CCLRC on behalf of PPARC. The Digitized Sky Survey was produced at the Space Telescope Science Institute under U.S. Government grant NAG W-2166. We have also made use of data products from the Midcourse Space Experiment (MSX). Original processing of the latter data was funded by the Ballistic Missile Defense Organization with additional support from NASA Office of Space Science. Guest User, Canadian Astronomy Data Centre, which is operated by the Dominion Astrophysical Observatory for the National Research Council of Canada's Herzberg Institute of Astrophysics.

REFERENCES

- Abergel, A. et al. 2002, *A&A*, 389, 239
- Abergel, A. et al. 2003, *A&A*, 410, 577
- Anthony-Twarog, B.J. 1982, *AJ*, 87, 1213
- Barnes, P.J., Crutcher, R.M., Bieging, J.H., Storey, J.W.V., & Willner, S.P. 1989, *ApJ*, 342, 883
- Barranco, J.A. & Goodman, A.A. 1998, *ApJ*, 504, 207
- Basu, S. & Ciolek, G.E. 2004, *ApJ*, in press
- Bik, A., Lenorzer, A., Kaper, L., Comerón, F., Waters, L.B.F.M., de Koter, A., & Hanson, M.M. 2003, *A&A*, 404, 249
- Beuther, H., Schilke, P., & Wyrowski, F. 2004, *ApJ*, in press
- Bonnor, W.B. 1956, *MNRAS*, 116, 351
- Carpenter, J.M. 2000, *AJ*, 120, 3139
- Clarke, C.J., Bonnell, I.A., & Hillenbrand, L.A. 2000, in *Protostars and Planets IV*, ed. V. Mannings, A. P. Boss & S. S. Russell (Tucson: University of Arizona Press), 151

- Ebert, R. 1955, *Zs.Ap.*, 37, 217
- Elmegreen, B.G., Efremov, Y, Pudritz, R.E., & Zinnecker, H. 2000, in *Protostars and Planets IV*, ed. V. Mannings, A. P. Boss & S. S. Russell (Tucson: University of Arizona Press), 179
- Evans, N.J. II 1999, *ARA&A*, 37, 311
- Fissel, L, Johnstone, D., Avery, L., & Mitchell, G.F. 2005, in preparation
- Friesen, R.K., Johnstone, D., Naylor, D.A., & Davis, G.R. 2005, *MNRAS*, submitted
- Goldsmith, P.F., Bergin, E.A., & Lis, D.C. 1997, *ApJ*, 491, 615
- Goodman, A.A., Barranco, J.A., Wilner, D.J., & Heyer, M.H. 1998, *ApJ*, 504, 223
- Grasdalen G.L. 1974, *ApJ*, 193, 373
- Hartmann, L. 1998, *Accretion Processes in Star Formation* (Cambridge: University Press)
- Hildebrand, R.H. 1983, *QJRAS*, 24, 267
- Hogerheijde, M.R. & Sandell, G. 2000, *ApJ*, 534, 880
- Holland, W.S. et al. 1999, *MNRAS*, 303, 659
- Jenness, T., Stevens, J.A., Archibald, E.N., Economou, F., Jessop, N.E., & Robson, E.I. 2002, *MNRAS*, 336, 14
- Johnstone, D., Di Francesco, J., & Kirk, H. 2004, *ApJ*611, L45
- Johnstone, D., Wilson, C.D., Moriarty-Schieven, G., Gainnakopoulou-Creighton, J., & Gregersen, E. 2000a (Paper I), *ApJS*, 131, 505
- Johnstone, D., Wilson, C.D., Moriarty-Schieven, G., Joncas, G., Smith, G., Gregersen, E., & Fich, M. 2000b (Paper II), *ApJ*, 545, 327
- Johnstone, D., Fich, M., Mitchell, G.F., & Moriarty-Schieven, G. 2001 (Paper III), *ApJ*, 559, 307
- Jørgensen, J.K., Schöier, F.L., & van Dishoeck, E.F. 2005, *astro-ph/0501623*
- Kerton, C.R., Martin, P.G., Johnstone, D., & Ballantyne, D.R. 2001, *ApJ*, 552, 601
- Kramer, C., Stutzki, J. & Winnewisser, G. 1996, *A&A*, 307, 915
- Kramer, C., Stutzki, J., Röhrig, R., & Corneliussen, U. 1998, *A&A*, 329, 249
- Kroupa, P., Tout, C. & Gilmore, G. 1993, *MNRAS*, 262,545
- Lada, E.A., Bally, J., & Stark, A.A. 1991a, *ApJ*, 368, 432
- Lada, E.A., DePoy, D.L., Evans II, N.J., & Gatley, I. 1991b, *ApJ*, 371, 171
- Lada, C.J. & Lada, E.A. 2003, *ARA&A*, 41, 57

- Launhardt, R., Mezger, P.G., Haslam, C.G.T., Kreysa, E., Lemke, R., Sievers, A. & Zylka, R. 1996, *A&A*, 312, 569
- Lenorzer, A., Mokiem, M.R., de Koter, A., & Puls, J. 2004, *A&A*, 422, 275
- Lombardi, M. & Alves, J. 2001, *A&A*, 377, 1023
- Mac Low, M. & Klessen, R.S. 2004, *Reviews of Modern Physics*, 76, 125
- Mangum, J.G., Wootten, A., & Barsony, M. 1999, *ApJ*, 526, 845
- McKee, C.F. & Williams, J.P. 1997, *ApJ*, 476, 144
- Mestel, L. & Spitzer, L. 1956, *MNRAS*, 116, 505
- Mezger, P.G., Chini, R., Kreysa, E., Wink, J.E., & Salter, C.J. 1988, *A&A*, 191, 44
- Miesch & Bally, J. 1994, *ApJ*, 429, 645
- Mitchell, G. F. 1993, in *Graduate Workshop on Star Formation*, eds. Arcoragi, J.-P., Bastien, P., and Pudritz, R. (Departement de Physique, Universite de Montreal), 81
- Mitchell, G.F., Johnstone, D., Moriarty-Schieven, G., Fich, M., & Tothill, N.F.H. 2001, *ApJ*, 556, 215
- Mookerjea, B., Ghosh, S.K., Rengarajan, T.N., Tandon, S.N. & Verma, R.P. 2000, *AJ*, 120, 1954
- Mookerjea, B., Kramer, C., Nielbock, M., & Nyman, L.-A. 2004, *A&A*, in press
- Motte, F., André, P., & Neri, R. 1998, *A&A*, 336, 150
- Motte, F., André, P., Ward-thompson, D., & Bontemps, S. 2001, *A&A*, 372L, 41
- Mouschovias, T.C. & Ciolek, G.E. 1999, *NATO ASIC Proc. 540: The Origin of Stars and Planetary Systems*, 305
- Nakano, T. 1984, *Fundamentals of Cosmic Physics*, 9, 139
- Onishi, T, Mizuno, A., Kawamura, A., Tachihara, K., & Fukui, Y. 2002, *ApJ*, 575, 950
- Pound, M.W., Reipurth, B. & Bally, J. 2003, *AJ*, 125, 2108
- Price, S.D., Egan, M.P., Carey, S.J., Mizuno, D.R., & Kuchar, T.A. 2001, *AJ*, 121, 2819
- Reid, M.A. & Wilson, C.D. 2005, *ApJ*, in press
- Reipurth, B., Rodríguez, L.F., Anglada, G., & Bally, J. 2004, *AJ*127, 1736
- Salpeter, E.E. 1955, *ApJ*, 121, 161
- Sandell, G. et al. 1999, *ApJ*, 519, 236
- Sandell, G., Jenness, T., McMullin, J.P. & Shah, R.Y. 2001, *BAAS*, 34, 562

- Scalo, J.M. 1985, *Protostars and Planets II*, 201
- Scalo, J. 1986, *Fundamentals of Cosmic Physics*, 11, 1
- Shu, F.H. 1983, *ApJ*, 273, 202
- Shu, F.H., Adams, F.C., & Lizano, S. 1987, *ARA&A*, 25, 23
- van der Tak, F.F.S., van Dishoeck, E.F., Evans, N.J. II, & Bakker, E.J.. 1999, *ApJ*, 522, 991
- Tafalla, M., Myers, P.C., Caselli, P., & Walmsley, C.M. 2004, *A&A*, 416, 191
- Testi, L. & Sargent, A.I. 1998, *ApJ*, 508, L91
- Teyssier, D., Fossé, D., Gerin, M., Pety, J., Abergel, A. & Roueff, E. 2004, *A&A*, 417, 135
- Visser, A.E., Richer, J.S., Chandler, C.J., & Padman, R. 1998, *MNRAS*, 301, 585
- Williams, J.P., Blitz, L, & McKee, C.F. 2000, in *Protostars and Planets IV*, ed. V. Mannings, A. P. Boss & S. S. Russell (Tucson: University of Arizona Press), 97
- Williams, J.P., de Geus, E.,J., & Blitz L. 1994, *ApJ*, 428, 693
- Williams, J.P. & McKee, C.F. 1997, *ApJ*, 476, 166

Table 1. Clump properties in Orion B South derived from 850 μm data.

Name ^a (SMM J)	R.A. ^b (J2000)	Dec. ^b (J2000)	S_{850} ^c (Jy)	S_{850}^{peak} ^c (Jy/bm)	R_{eff} ^c (10^3 AU)	C^{d}	T_d^{d} (K)	$\log P/k^{\text{d}}$ (K/cm ³)	$M_{T_d^{\text{d}}}$ (M_{\odot})	$M_{T_d=20\text{K}}^{\text{e}}$ (M_{\odot})
054086-01528	05:40:51.8	-01:52:48	1.23	0.18	11	0.40	18	6.0	1.15	0.98
054089-02271	05:40:53.4	-02:27:06	2.18	0.31	12	0.51	16	6.0	2.44	1.73
054090-01531	05:40:54.0	-01:53:06	0.89	0.21	9	0.42	16	6.2	1.00	0.71
054091-02278	05:40:54.6	-02:27:51	2.90	0.28	14	0.45	19	6.0	2.49	2.31
054096-02074	05:40:57.6	-02:07:27	2.18	0.28	13	0.54	15	5.9	2.72	1.73
054097-02086	05:40:58.2	-02:08:36	4.21	0.40	16	0.57	18	5.9	3.92	3.34
054100-02092	05:40:59.8	-02:09:15	5.24	0.29	19	0.52	19	5.8	4.49	4.16
054105-01558	05:41:03.2	-01:55:51	1.43	0.20	11	0.45	16	6.0	1.60	1.13
054112-02273	05:41:07.0	-02:27:18	3.08	0.48	13	0.61	16	6.0	3.46	2.45
054116-01580	05:41:09.4	-01:58:00	1.25	0.24	10	0.48	15	6.1	1.56	0.99
054140-01507	05:41:23.8	-01:50:45	0.96	0.27	9	0.52	13	6.1	1.53	0.76
054141-02180	05:41:24.8	-02:18:03	18.57	3.19	21	0.87	25	5.9	10.72	14.74
054141-02289	05:41:24.4	-02:28:54	0.76	0.21	8	0.44	15	6.2	0.95	0.60
054142-02160	05:41:25.2	-02:16:00	7.42	0.47	20	0.60	19	5.8	6.36	5.89
054142-02194	05:41:25.4	-02:19:24	4.18	0.48	14	0.55	19	6.1	3.58	3.32
054146-02208	05:41:27.8	-02:20:51	2.36	0.29	12	0.45	19	6.1	2.03	1.88
054146-02239	05:41:27.6	-02:23:54	1.90	0.26	12	0.50	16	6.0	2.13	1.51
054148-02200	05:41:28.6	-02:20:03	4.92	0.48	15	0.54	20	6.1	3.91	3.91
054149-02212	05:41:29.4	-02:21:15	5.36	0.97	15	0.77	17	5.8	5.46	4.26
054149-02232	05:41:29.2	-02:23:15	0.83	0.25	8	0.50	13	6.2	1.33	0.66
054151-02251	05:41:30.4	-02:25:06	0.91	0.19	9	0.38	21	6.1	0.68	0.73
054152-02262	05:41:31.0	-02:26:12	3.45	0.21	17	0.45	19	5.8	2.96	2.74
054153-02189	05:41:31.6	-02:18:57	4.56	0.32	18	0.56	17	5.8	4.64	3.62
054155-01497	05:41:33.2	-01:49:45	1.87	0.32	10	0.46	18	6.2	1.74	1.49
054156-02209	05:41:33.4	-02:20:54	1.16	0.25	9	0.47	15	6.1	1.45	0.92
054156-02250	05:41:33.6	-02:25:03	0.78	0.18	9	0.42	16	6.1	0.88	0.62
054158-01558	05:41:34.8	-01:55:48	4.15	0.40	15	0.54	18	6.0	3.87	3.30
054158-02303	05:41:34.6	-02:30:18	0.47	0.19	6	0.39	16	6.3	0.52	0.37
054159-01514	05:41:35.6	-01:51:27	2.01	0.34	11	0.51	16	6.1	2.26	1.60
054160-01492	05:41:35.8	-01:49:12	1.14	0.41	8	0.54	14	6.3	1.60	0.90
054160-01564	05:41:35.8	-01:56:24	15.16	0.58	24	0.53	26	5.9	8.29	12.03
054160-02300	05:41:36.0	-02:30:00	0.49	0.18	7	0.36	21	6.3	0.36	0.39
054161-01495	05:41:36.6	-01:49:30	1.58	0.44	9	0.54	15	6.3	1.97	1.25
054162-02172	05:41:37.0	-02:17:15	19.86	1.66	26	0.82	24	5.7	12.13	15.76
054163-01509	05:41:37.8	-01:50:54	2.18	0.34	11	0.46	18	6.2	2.03	1.73
054163-01558	05:41:37.6	-01:55:48	7.46	0.58	15	0.44	28	6.2	3.69	5.92
054164-01504	05:41:38.4	-01:50:24	1.48	0.28	10	0.44	18	6.2	1.38	1.17
054167-02171	05:41:40.2	-02:17:06	13.91	1.12	17	0.59	27	6.2	7.23	11.04
054170-02162	05:41:42.0	-02:16:12	12.06	0.68	23	0.65	21	5.7	8.91	9.57
054172-01543	05:41:43.0	-01:54:21	85.03	11.11	24	0.86	47	6.4	21.96	67.50
054173-01527	05:41:44.0	-01:52:45	18.04	0.85	24	0.64	25	5.8	10.41	14.32
054173-01547	05:41:44.0	-01:54:42	63.67	7.99	23	0.85	42	6.3	18.82	50.54
054173-02170	05:41:43.8	-02:17:03	7.67	0.49	20	0.60	20	5.8	6.09	6.09
054174-01556	05:41:44.4	-01:55:39	90.41	15.35	19	0.83	54	6.7	19.82	71.77
054175-01560	05:41:45.0	-01:56:00	113.37	10.15	29	0.87	49	6.2	27.86	90.00

Table 1—Continued

Name ^a (SMM J)	R.A. ^b (J2000)	Dec. ^b (J2000)	S_{850} ^c (Jy)	S_{850}^{peak} ^c (Jy/bm)	R_{eff} ^c (10^3 AU)	C ^d	T_d ^d (K)	$\log P/k$ ^d (K/cm ³)	M_{T_d} ^d (M_{\odot})	$M_{T_d=20\text{ K}}$ ^e (M_{\odot})
054182-01576	05:41:49.4	-01:57:39	24.19	1.07	27	0.69	26	5.7	13.23	19.21
054182-01596	05:41:49.2	-01:59:36	3.58	0.47	14	0.63	16	5.9	4.02	2.84
054185-01534	05:41:51.2	-01:53:27	0.66	0.19	8	0.42	15	6.2	0.83	0.53
054188-02002	05:41:53.0	-02:00:12	1.11	0.30	8	0.45	16	6.3	1.24	0.88
054190-02004	05:41:54.0	-02:00:24	0.95	0.31	8	0.48	15	6.3	1.18	0.75
054192-01565	05:41:55.0	-01:56:33	4.86	0.22	19	0.40	26	5.8	2.66	3.86
054195-02009	05:41:56.8	-02:00:54	0.50	0.25	6	0.48	13	6.4	0.80	0.40
054204-02077	05:42:02.4	-02:07:42	3.09	0.95	12	0.76	16	6.0	3.47	2.45
054205-02025	05:42:02.8	-02:02:33	3.89	1.14	11	0.72	18	6.2	3.62	3.09
054207-02017	05:42:04.2	-02:01:42	0.72	0.19	8	0.40	17	6.2	0.73	0.57
054207-02032	05:42:04.0	-02:03:12	0.58	0.21	7	0.44	14	6.3	0.81	0.46
054218-02042	05:42:10.8	-02:04:12	0.95	0.30	9	0.56	13	6.2	1.51	0.75

^aName formed from J2000 positions (hhmm.mmddmm.m).

^bPosition of peak surface brightness within clump (accurate to 3").

^cRadius, peak flux, and total flux are derived from *clfind* (Williams et al. 1994). The peak flux and total flux have uncertainties of about 20 percent, mostly due to absolute flux calibration. The radius has not been deconvolved from the telescope beam.

^dQuantities derived from Bonnor-Ebert analysis (see text).

^eMass derived from the total flux assuming $T_d = 20$ K and $\kappa_{850} = 0.02 \text{ cm}^2 \text{ g}^{-1}$.

Table 2. Submillimeter wavelength properties of clumps in Orion B South

Name ^a (SMM J)	S_{450}/S_{850} ^b	$S_{450}^{\text{peak}}/S_{850}^{\text{peak}}$ ^b	$T_d(\text{BE})$ ^c (K)	$T_d(\text{SM})$ ^d (K)
054086-01528	24.4	23.5	18	50
054089-02271	8.2	7.9	16	21
054090-01531	20.8	16.6	16	50
054091-02278	9.4	8.7	19	28
054096-02074	10.0	9.7	15	35
054097-02086	8.6	8.3	18	22
054100-02092	8.6	8.6	19	23
054105-01558	12.4	11.0	16	50
054112-02273	10.5	8.7	16	43
054116-01580	2.9	5.7	15	7
054140-01507	8.0	10.5	13	19
054141-02180	7.5	5.7	25	17
054141-02289	13.1	12.1	15	50
054142-02160	8.4	8.4	19	21
054142-02194	5.4	6.5	19	12
054146-02208	6.9	7.9	19	15
054146-02239	11.5	10.2	16	50
054148-02200	6.4	7.2	20	14
054149-02212	8.0	6.7	17	20
054149-02232	8.9	8.3	13	24
054151-02251	12.0	13.0	21	50
054152-02262	7.9	9.9	19	19
054153-02189	2.9	4.5	17	7
054155-01497	8.0	9.2	18	19
054156-02209	6.1	7.7	15	13
054156-02250	13.1	14.1	16	50
054158-01558	11.8	12.5	18	50
054158-02303	11.6	11.8	16	50
054159-01514	13.0	11.4	16	50
054160-01492	6.7	9.9	14	15
054160-01564	15.5	19.4	26	50
054160-02300	13.0	12.3	21	50
054161-01495	9.6	10.4	15	29
054162-02172	6.8	5.0	24	15
054163-01509	13.3	12.2	18	50

Table 2—Continued

Name ^a (SMM J)	S_{450}/S_{850} ^b	$S_{450}^{\text{peak}}/S_{850}^{\text{peak}}$ ^b	$T_d(\text{BE})$ ^c (K)	$T_d(\text{SM})$ ^d (K)
054163-01558	17.5	18.9	28	50
054164-01504	10.4	10.9	18	40
054167-02171	8.5	9.1	27	22
054170-02162	6.0	8.5	21	13
054172-01543	14.0	11.2	47	50
054173-01527	15.2	16.5	25	50
054173-01547	13.9	11.5	42	50
054173-02170	6.1	8.4	20	13
054174-01556	12.8	9.8	54	50
054175-01560	16.3	12.4	49	50
054182-01576	22.4	17.7	26	50
054182-01596	19.3	13.9	16	50
054185-01534	18.5	24.2	15	50
054188-02002	17.6	15.6	16	50
054190-02004	17.3	15.8	15	50
054192-01565	23.4	29.4	26	50
054195-02009	15.1	12.4	13	50
054204-02077	7.9	6.9	16	19
054205-02025	11.3	9.9	18	50
054207-02017	13.5	14.8	17	50
054207-02032	10.9	14.3	14	50
054218-02042	7.6	8.6	13	18

^aName formed from J2000 positions (hhmm.mmddmm.m).

^bThe 850 μm and 450 μm peak flux and total flux are derived from *clfind* (Williams et al. 1994) after convolution to an identical beam size.

^cQuantity derived from Bonnor-Ebert analysis (see text).

^dQuantity derived from spectral energy fit to 450 and 850 μm integrated fluxes (see text).

Table 3. Dust and gas properties of clumps in NGC 2023

Name ^a (SMM J)	T_d (BE) (K)	T_d (SM) (K)	$T_{\text{gas}}(\text{C}^{18}\text{O})$ (K)	$N(850)^b$ (10^{22} cm^{-2})	$N(\text{C}^{18}\text{O})$ (10^{22} cm^{-2})	$N(850)/N(\text{C}^{18}\text{O})$
054141-02180	25	19	18	12.1	3.4	3.6
054153-02189	17	8	14	2.1	4.2	0.5
054162-02172	24	16	18	6.6	4.9	1.3
054167-02171	27	24	25	3.8	10.0	0.4
054173-02170	20	14	15	2.6	5.8	0.4

^aName formed from J2000 positions (hhmm.mmddmm.m).

^bColumn density derived assuming the BE temperature for the dust.

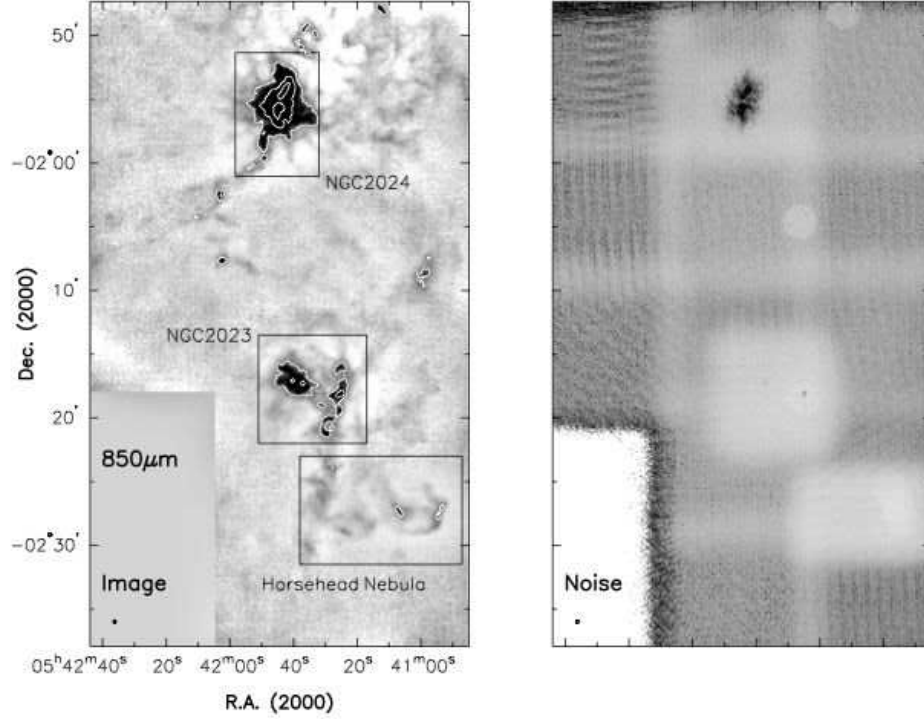


Fig. 1.— The Orion B South region at $850\ \mu\text{m}$. North to south, the bright star-forming regions are: NGC 2024, NGC 2023, and the Horsehead. Left: $850\ \mu\text{m}$ emission (greyscale: white to black represents -0.25 to $0.5\ \text{Jy}\ \text{beam}^{-1}$, contours are shown for 0.25 , 1 , and $4\ \text{Jy}\ \text{beam}^{-1}$). The named boxes indicate the regions displayed in Figures 4 to 6. The beamsize is noted in the lower left of the figure. Right: $850\ \mu\text{m}$ noise map (greyscale: white to black represents 0 to $0.15\ \text{Jy}\ \text{beam}^{-1}$). In the noise map, the lower right hand corner has a slightly higher than typical uncertainty of $0.07\ \text{Jy}\ \text{pixel}^{-1}$ while the Horsehead region directly above has a typical uncertainty of $0.03\ \text{Jy}\ \text{pixel}^{-1}$. The greater noise in regions where there is strong signal, such as NGC 2024, is due to uncertainties in the calibration of individual bolometers.

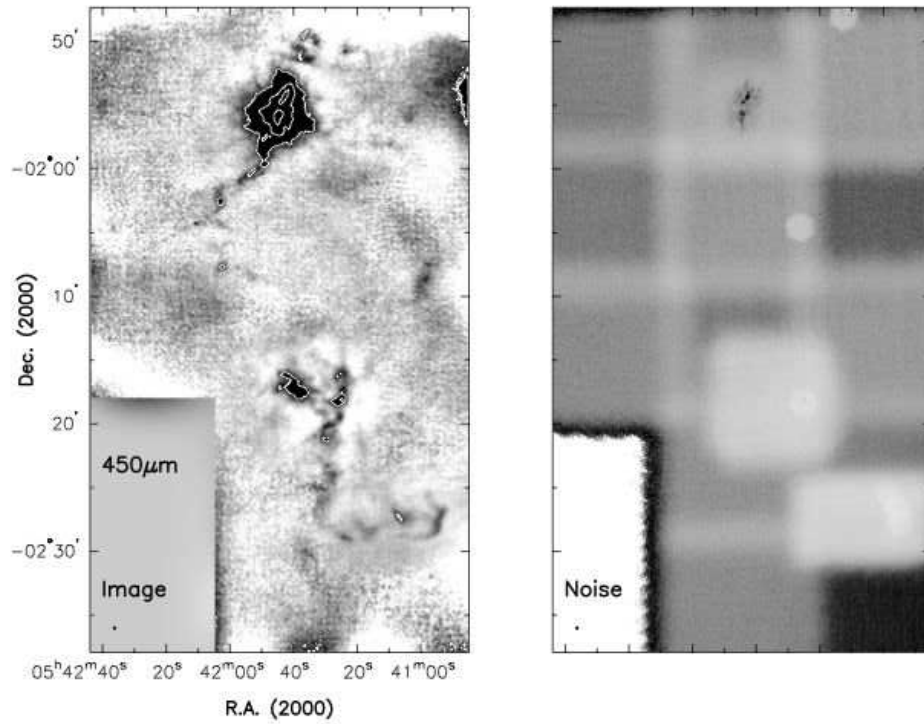


Fig. 2.— The Orion B South region at $450 \mu\text{m}$, covering the same area as described in Figure 1. Left: $450 \mu\text{m}$ emission (greyscale: white to black represents -1 to 2 Jy bm^{-1} , contours at $2, 8, 32 \text{ Jy bm}^{-1}$). The beamsize is noted in the lower left of the figure. Right: $450 \mu\text{m}$ noise map (greyscale: white to black represents 0 to 1 Jy bm^{-1}). In the noise map, the lower right hand corner reveals a higher than typical uncertainty of $0.9 \text{ Jy pixel}^{-1}$ while the Horsehead region directly above has a typical uncertainty of $0.2 \text{ Jy pixel}^{-1}$.

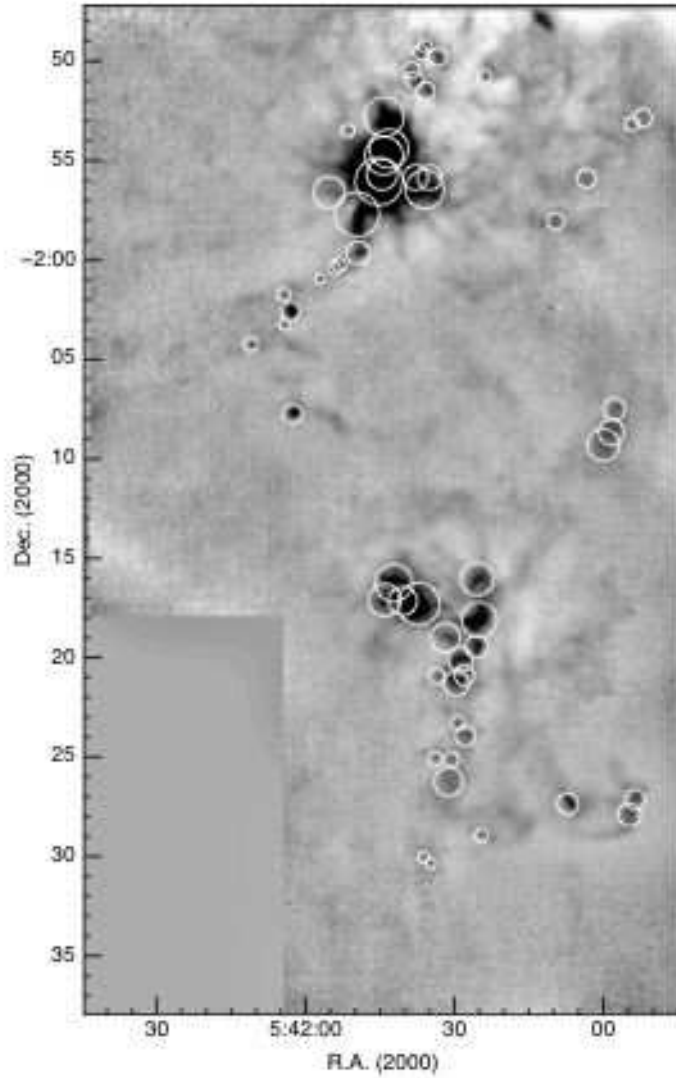


Fig. 3.— Location of the submillimeter clumps found in Orion B South $850\ \mu\text{m}$ using an automated procedure (see text). The circle size approximates the area associated with each clump.

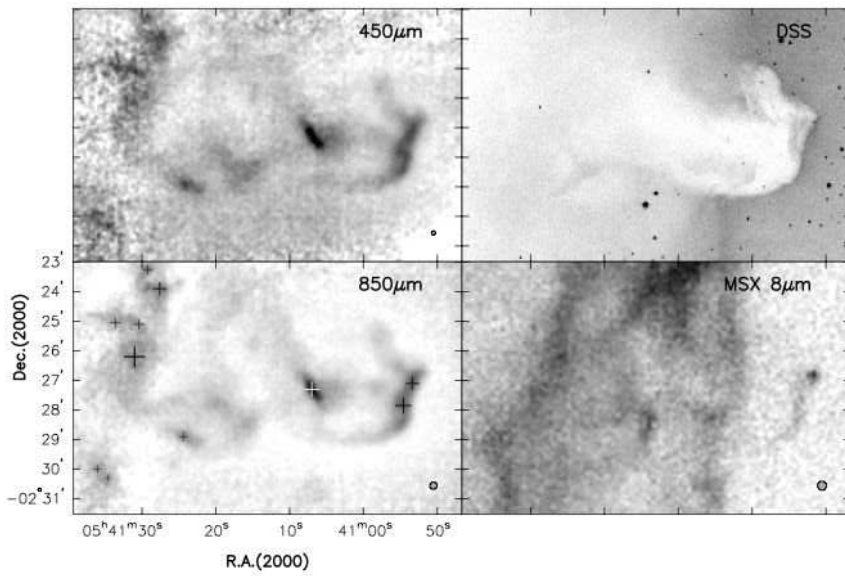


Fig. 4.— The Horsehead Nebula region (B33). The panels show the 450 and 850 μm emission at upper and lower left respectively, plotted on intensity scales chosen to illustrate the structure of the emission to good advantage. Overlaid on the 850 μm map are plus-signs denoting the locations of the submillimeter sources. At upper right we show the corresponding image from the Digitized Sky Survey (DSS), and at lower right an image from the 8- μm data obtained from the MSX database. The small circle at lower right in each case indicates the respective beamwidths, except for the DSS data.

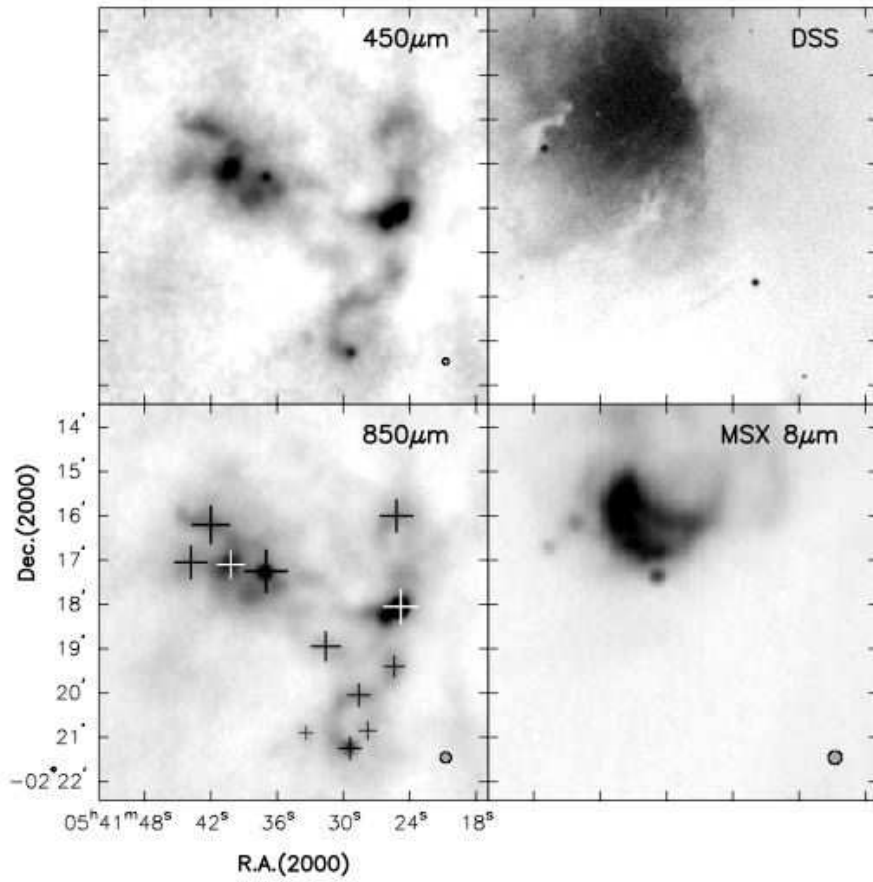


Fig. 5.— The NGC 2023 region at submillimeter (left), optical (upper right) and mid-infrared (lower right) wavelengths. Other details are as for Figure 4.

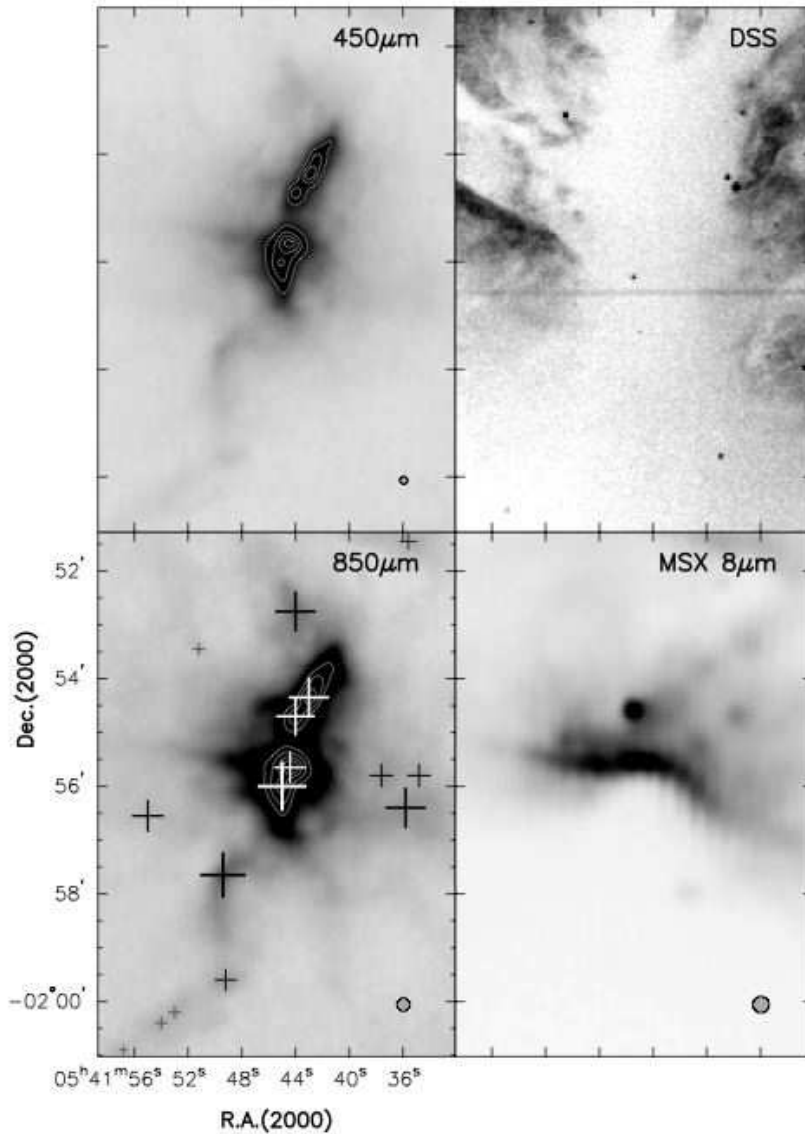


Fig. 6.— The NGC 2024 region at submillimeter (left), optical (upper right) and mid-infrared (lower right) wavelengths. The horizontal stripe in the DSS image is due to a bright star outside the frame shown here. Vertical banding in the MSX image is an artifact. Additional contours for the $450 \mu\text{m}$ image are 30, 45, 60 and 75 Jy/beam area , and for the $850 \mu\text{m}$ image are 4, 6, 9, 12 and 15 Jy/beam area . Other details are as for Figure 4.

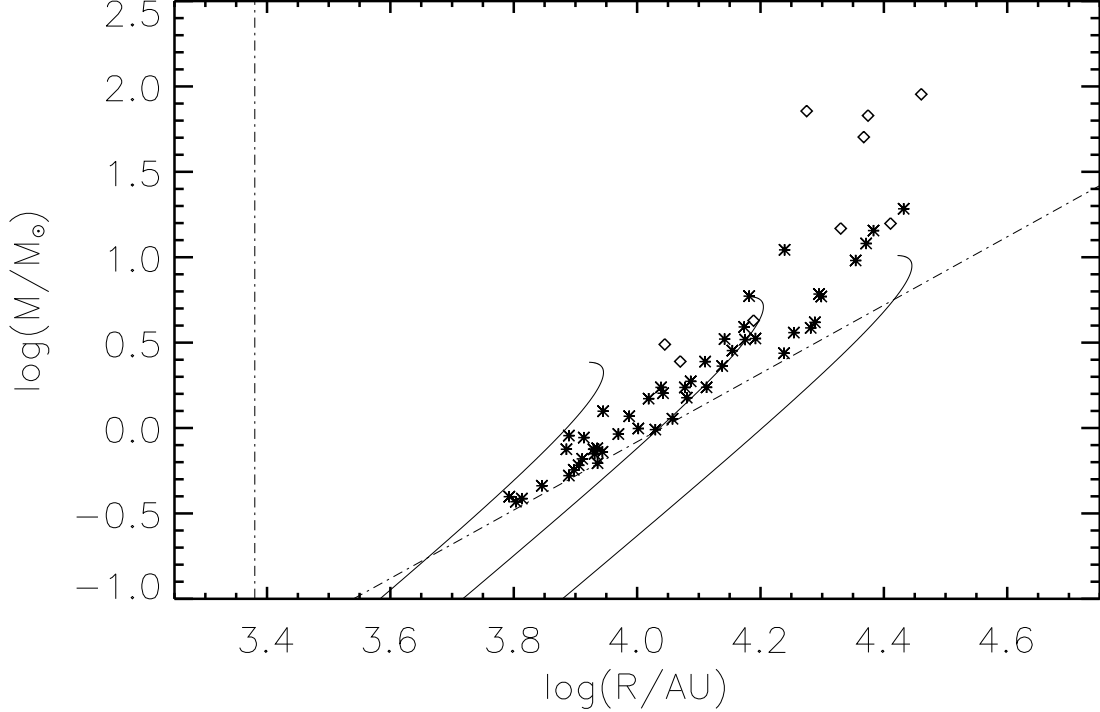


Fig. 7.— Derived mass for each of the 57 clumps, assuming $T_d = 20$ K, versus the effective radius. Note that the effective radius is derived from the extent of the clump as determined by `clfind` (see text) and the largest uncertainty in the mass of the clump is the flux calibration, which is accurate to about twenty percent. Also plotted (dashed-dotted) are the minimum size which a clump might have (resolution limit) and the minimum mass that a clump must have for a given radius such that the clump-finding routine can recognize it (approximately 4σ above the background). The symbols denoting each clump are discussed in Figure 8. The three curves from left to right denote the mass-radius relation for Bonnor-Ebert spheres with 20 K internal temperatures, an additional equal internal pressure component due to turbulence, and external pressures $k^{-1}P = 0.3, 1.0, 3.3 \times 10^6$ K cm $^{-3}$ (see text).

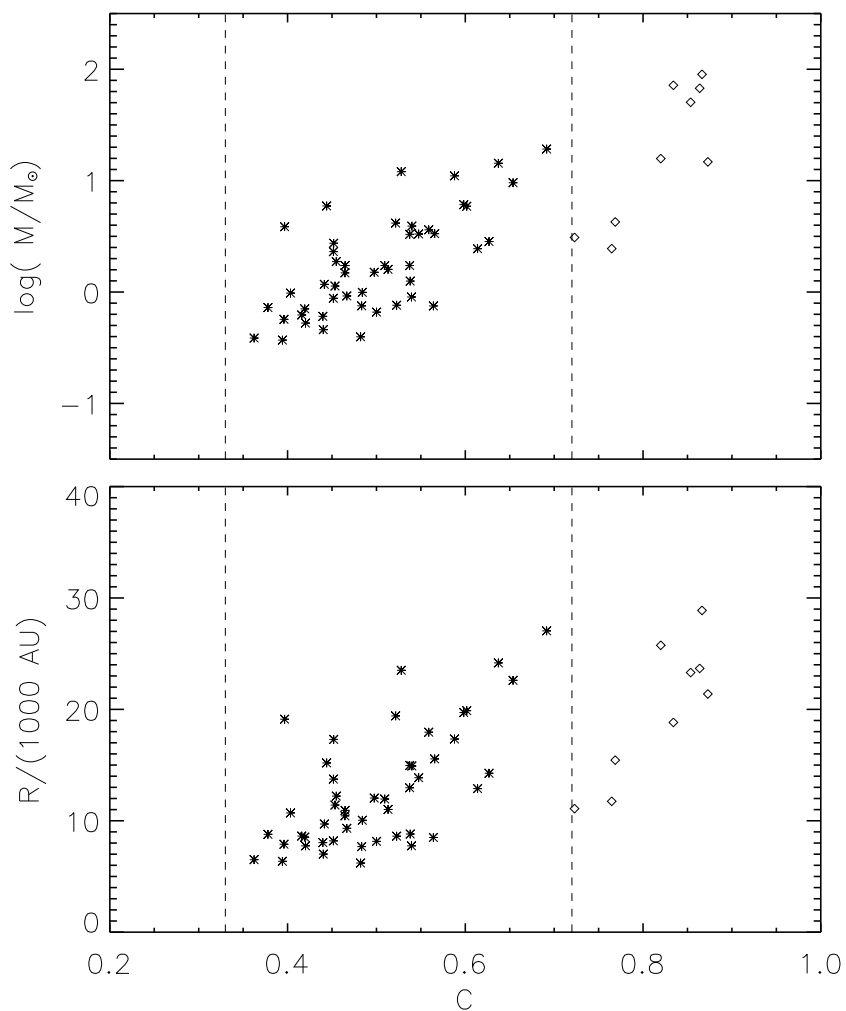


Fig. 8.— Derived concentration for each of the 57 clumps in the Orion B South region (see text). The minimum concentration for a constant density low-mass Bonnor-Ebert sphere is $C = 0.33$, while the maximum concentration beyond which collapse occurs is $C = 0.72$. Clumps with $C > 0.72$ are denoted by diamonds. (Top) Derived mass of the clump, assuming $T_d = 20$ K, vs. concentration. (Bottom) Derived radius of the clump vs. concentration.

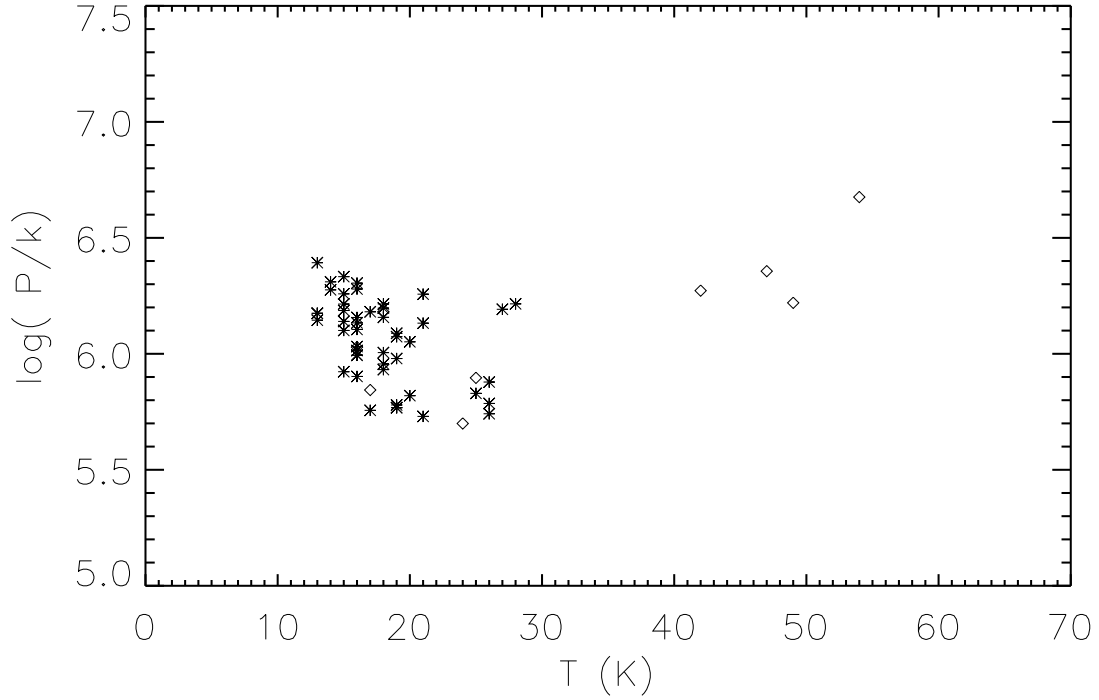


Fig. 9.— Results of determining the physical parameters of clumps using the assumption that they are well represented by Bonnor-Ebert spheres with measured concentrations. Plotted are the external, confining pressure vs. the internal temperature (assuming an equal contribution from turbulent support). The typical uncertainty in the derived physical parameters of an individual clump is similar to the spread in the distribution of points. The symbols are the same as in Fig. 8.

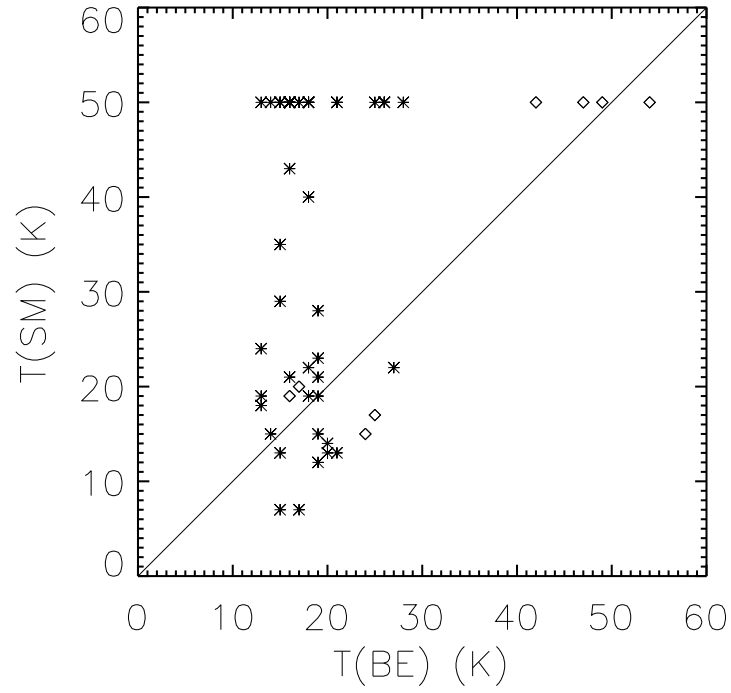


Fig. 10.— Comparison of the clump temperature derived from the Bonnor-Ebert analysis versus the clump temperature derived from spectral energy fitting between the $450\ \mu\text{m}$ and $850\ \mu\text{m}$ observations (see text).

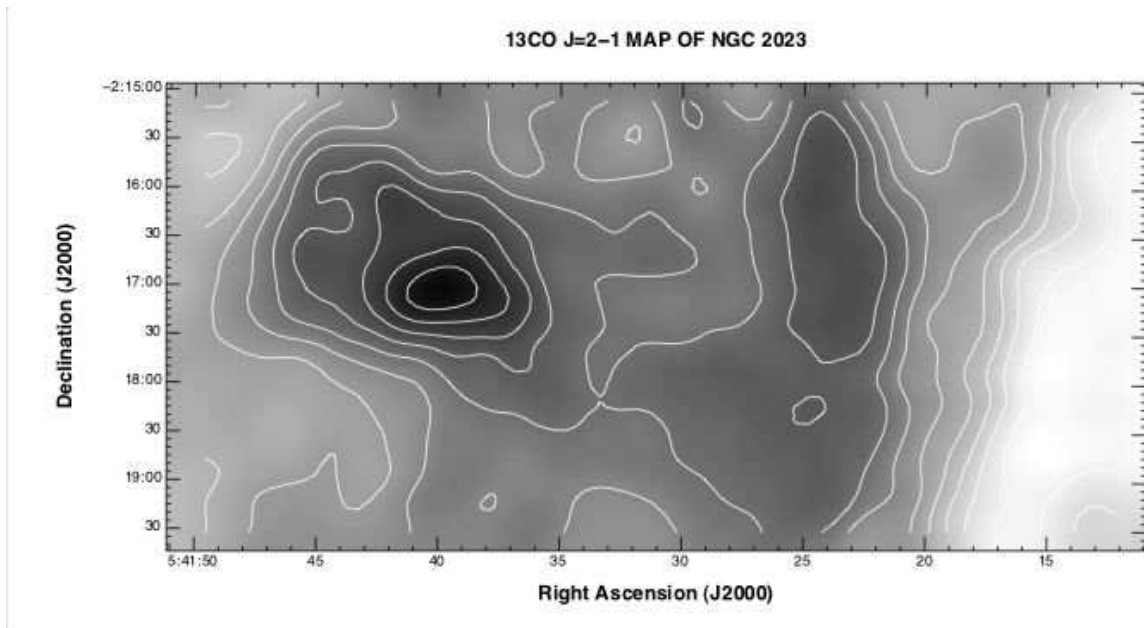


Fig. 11.— A ^{13}CO $J = 2-1$ raster map of NGC 2023. The beam size is $21''$. The sampling interval is $7.5''$ in R.A. and Dec. The maximum contour is 58.0 K.km/s and the contour interval is 5.0 K.km/s.

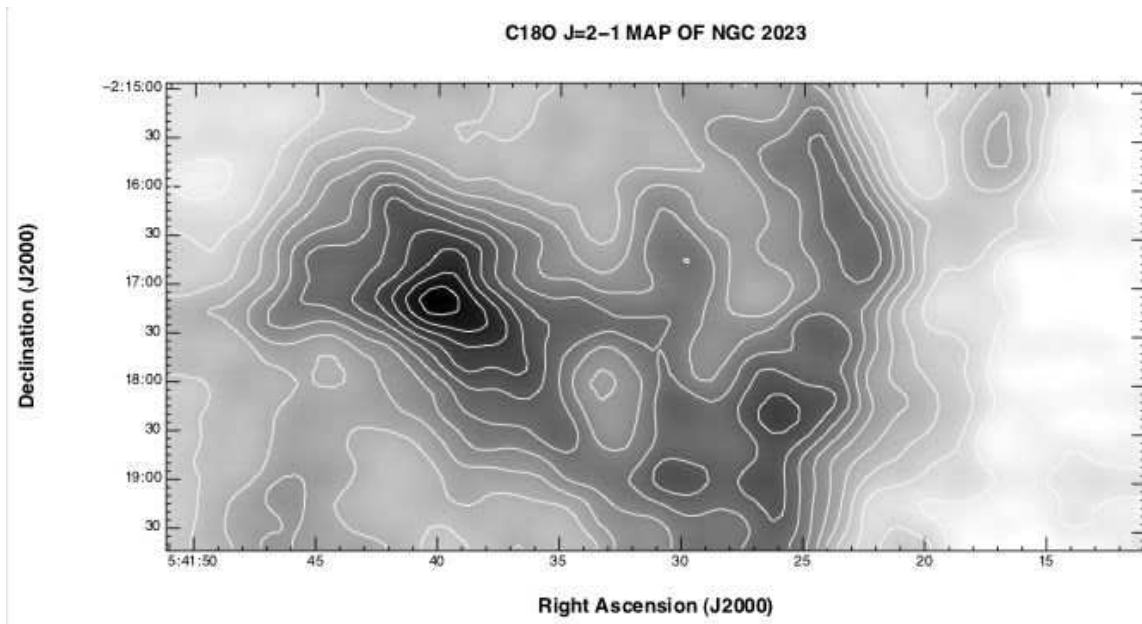


Fig. 12.— A C^{18}O $J = 2-1$ raster map of NGC 2023. The beam size is $21''$. The sampling interval is $7.5''$ in R.A. and Dec. The ^{13}CO $J = 2-1$ and C^{18}O $J = 2-1$ maps were obtained simultaneously with a single tuning of the facility A-band receiver. The maximum contour is 12.3 K.km/s and the contour interval is 1.0 K.km/s

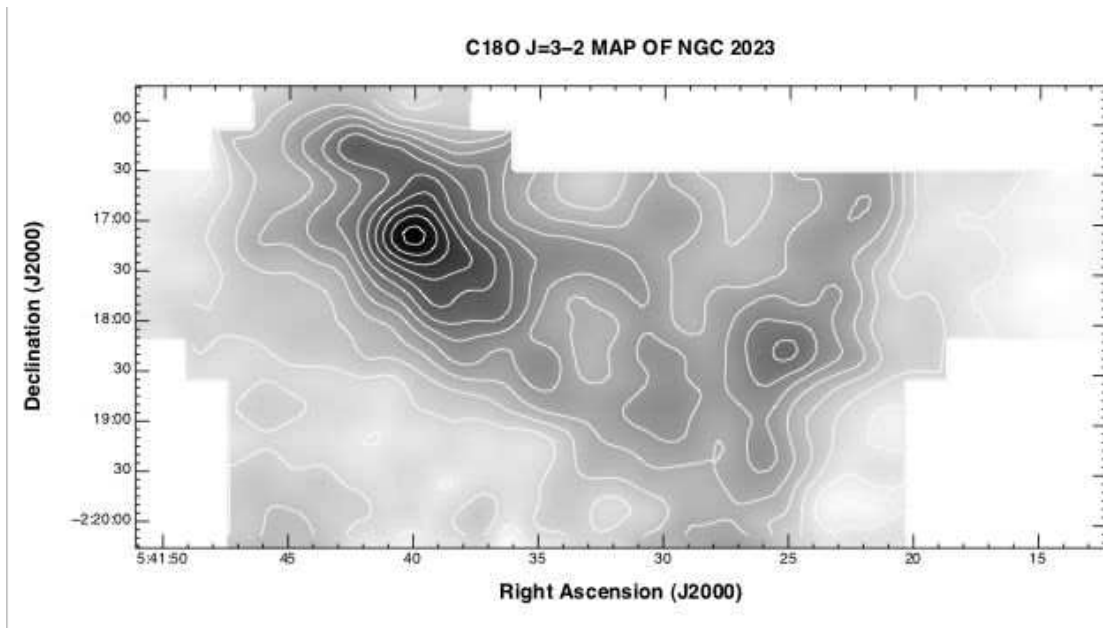


Fig. 13.— A C^{18}O $J = 3-2$ raster map of NGC 2023. The beam size is $14''$. The sampling interval is $5''$ in R.A. and Dec. The maximum contour is 13.4 K.km/s and the contour interval is 1.0 K.km/s .

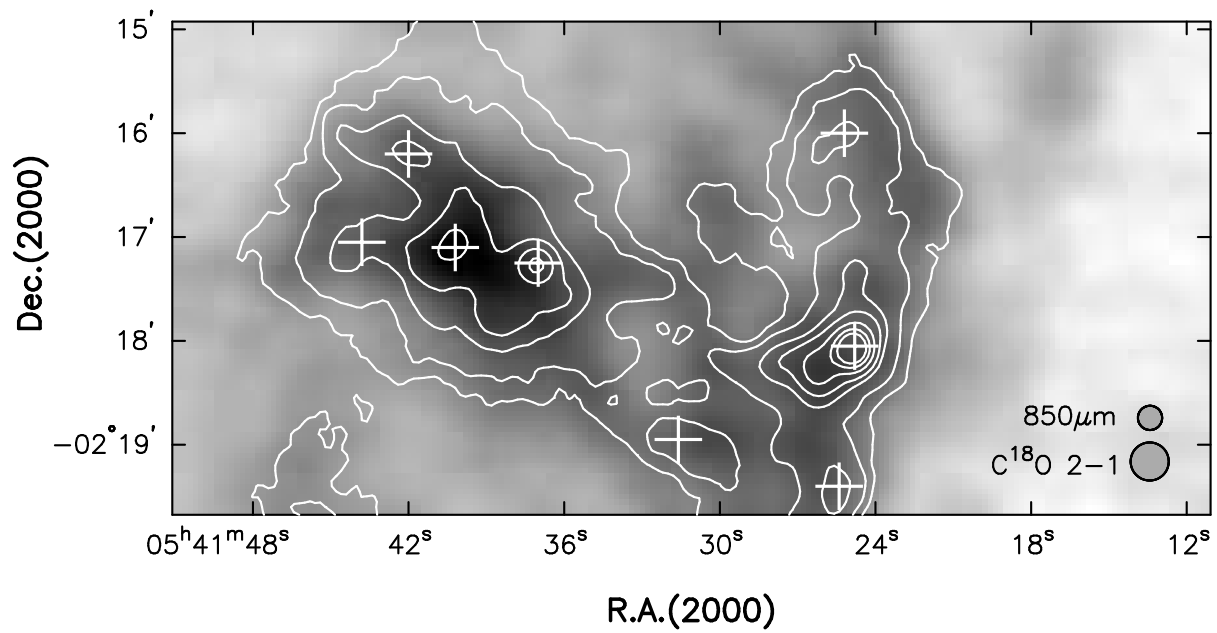


Fig. 14.— The C¹⁸O J = 2–1 grayscale image of NGC 2023 (see Figure 12), overlain by contours of the 850 μm continuum emission. The contour levels shown are 0.1, 0.2, 0.4, 0.6, 1.0, 1.5, and 2.0 Jy/beam, and the beamsizes to half-power are indicated at lower right. The superposed crosses show the locations of the continuum sources indicated by the automated clump-finding routine (see Section 3.1, and also Figures 3 and 5).

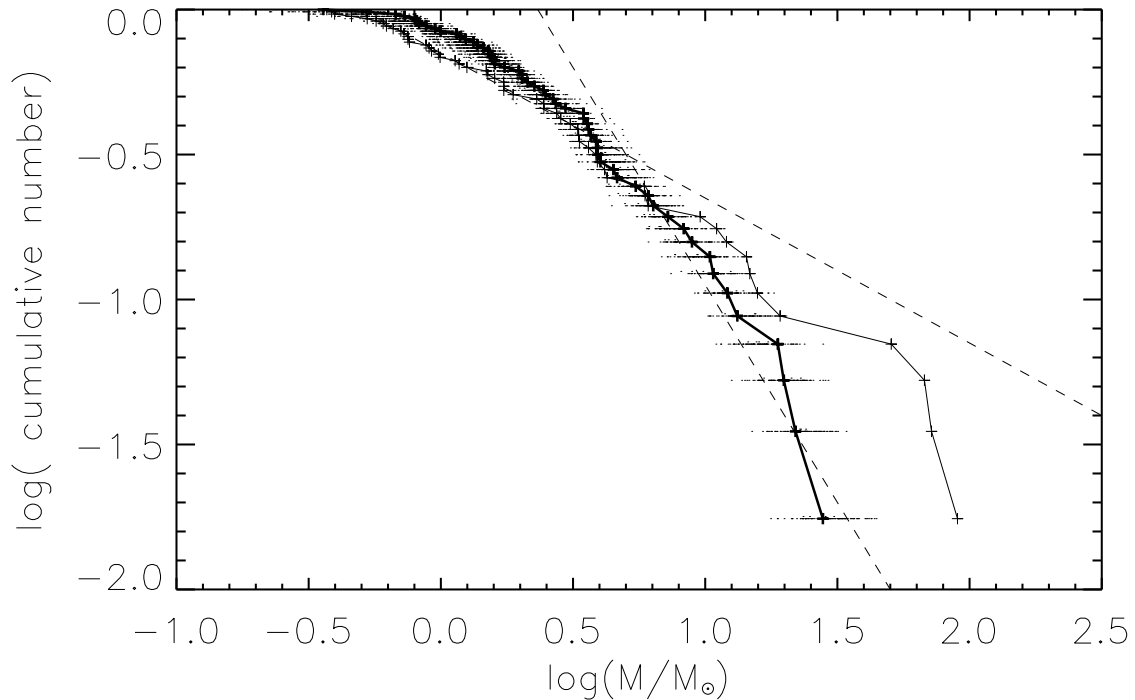


Fig. 15.— Cumulative number function for the $850\ \mu\text{m}$ clumps in Orion B South. The thin line converts the measured flux directly to mass using a constant temperature $T_d = 20\ \text{K}$. The thick line converts the flux to mass using the derived temperature from fitting the clumps to Bonnor-Ebert spheres (see text). The horizontal lines represent the extent to which the masses might change due to uncertainties in the Bonnor-Ebert Measurements (see Paper III). The steep dashed line has a slope $M^{-1.5}$ and approximates the high-mass end of the Bonnor-Ebert cumulative distribution. The shallow dashed line has a slope $M^{-0.5}$ and approximates the low-mass end of the distribution. The low-mass end is likely to be severely incomplete (see text).

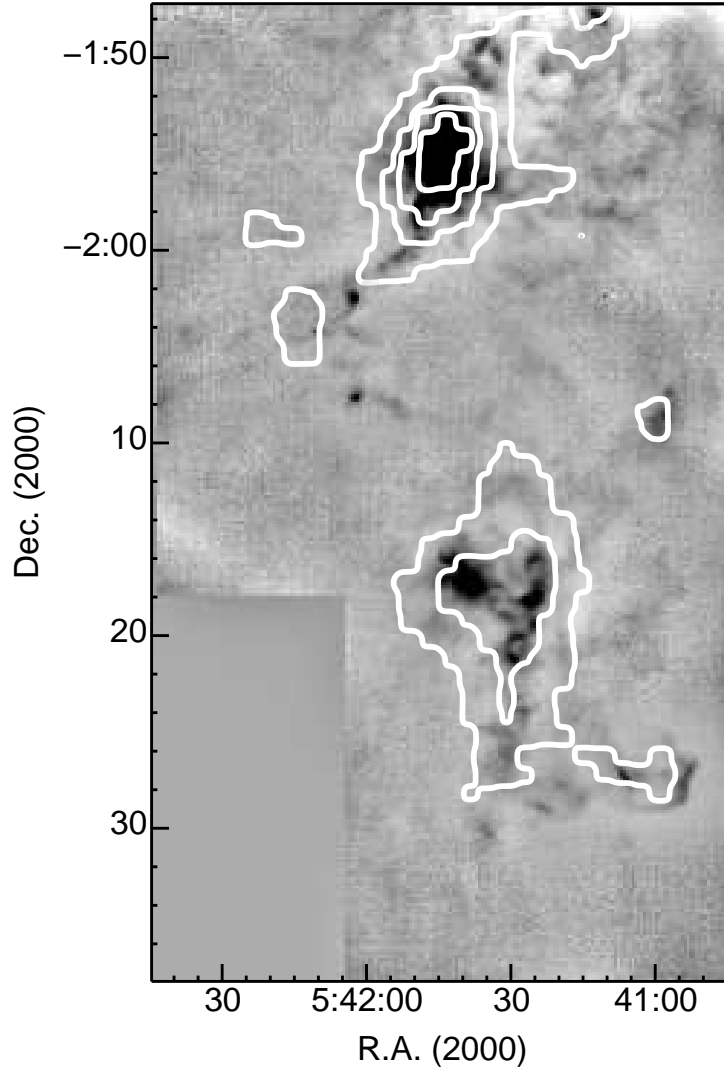


Fig. 16.— Contours of CS $J = 2-1$ emission (from Lada et al. 1991) are overlaid on the $850\ \mu\text{m}$ map. The contour levels are at 1.5 , 3.0 , 6.0 , and $12.0\ \text{K km s}^{-1}$. Note that a majority of the strong dust continuum sources lie above the $3\ \text{K km s}^{-1}$ contour.